https://ntrs.nasa.gov/search.jsp?R=19690030669 2020-03-23T19:55:19+00:00Z

General Disclaimer

One or more of the Following Statements may affect this Document

- This document has been reproduced from the best copy furnished by the organizational source. It is being released in the interest of making available as much information as possible.

- This document may contain data, which exceeds the sheet parameters. It was furnished in this condition by the organizational source and is the best copy available.

- This document may contain tone-on-tone or color graphs, charts and/or pictures, which have been reproduced in black and white.

- This document is paginated as submitted by the original source.

- Portions of this document are not fully legible due to the historical nature of some of the material. However, it is the best reproduction available from the original submission.

Produced by the NASA Center for Aerospace Information (CASI)

DEVELOPMENT OF A SKIN-FRICTION BALANCE TO INVESTIGATE SOURCES OF ERROR IN DIRECT SKIN-FRICTION MEASUREMENTS

A Thesis

Presented to

the Faculty of the School of Engineering and Applied Science

University of Virginia

In Partial Fulfillment

of the Requirements for the Degree

Master of Mechanical Engineering

---

by

James G. Fowke

June 1969

N69-40054
(ACCESSION NUMBER) 72 (PAGES)
(THRU) 1 (CODE) 14 (CATEGORY)
TMX-61905 (NASA CR OR TMX OR AD NUMBER)
FACILITY FORM 602

NOV 1969
RECEIVED
NASA STI FACILITY
INPUT BRANCH

APPROVAL SHEET

This thesis is submitted in partial fulfillment of

the requirements for the degree of

Master of Mechanical Engineering

_____

Author

Approved:

_____

Faculty Advisor

_____

Dean, School of Engineering and
Applied Science

June 1969

ACKNOWLEDGMENTS

The author extends his appreciation to those persons whose cooperation and services have made this thesis possible. Acknowledgment is given to Mr. Joseph F. Guarino for his guidance and encouragement in the subject matter, also to Mr. John B. Peterson, Jr., who provided information with regard to the need and application of the skin-friction balance. Indebtedness is extended to the National Aeronautics and Space Administration, Langley Research Center, which supported this effort.

TABLE OF CONTENTS

CHAPTER PAGE

LIST OF TABLES

LIST OF FIGURES

FIGURE PAGE

LIST OF SYMBOLS

A	area, ft^2
A(s)	loop gain function
a	constant coefficient
Btu	British thermal units
C	damping coefficient, lb-in.-sec/rad
d	diameter, in.
E_ℓ	LVDT output, volt
E_m	motor voltage, volt
E_r	reference voltage, volt
E_s	feedback voltage, volt
E_t	tachometer voltage, volt
F_a	applied force, lb
F_m	motor force, lb
f(s)	a function of frequency
f(t)	a function of time
G(s)	forward loop transfer function
h	height, in.
H(s)	feedback loop transfer function
I, i	current, ampere
J	polar moment of inertia, lb-in.-sec^2/rad
j	imaginary quantity
k	coefficient of thermal conductivity, Btu-in./hr-ft^2-^oF

K	flexure spring constant, lb-in./rad
K_i	integral-plus-proportional control amplifier gain, 1/sec
K_ℓ	LVDT scale factor, volt/in.
K_m	force motor scale factor, lb/amp
K_s	servo amplifier gain
K_t'	tachometer amplifier gain
K_t	tachometer scale factor, volt-sec/in.
K_v	motor (tachometer) back emf, volt-sec/in.
L	arm length, in.
L_l	arm length from LVDT axis to pivot axis, in.
mV	millivolt
P_t	stagnation pressure, psig
PM	phase margin, degrees
q	heat flow, Btu/hr
R	resistance, ohms
s	Laplace transform operator
T	temperature, ^oF
T_t	stagnation temperature, ^oF
t	time, sec
x	thickness, in.
ΔT	temperature difference, ^oF
θ	angular displacement, rad
$\dot{\theta}$	angular speed, rad/sec
$\ddot{\theta}$	angular acceleration, rad/sec^2
τ	time constant, sec

μ	micro, 10^{-6}
ω	frequency, rad/sec
ω_c	crossover frequency, rad/sec

ABSTRACT

The development of a force transducer for use in wind tunnels to study attendant errors associated with skin-friction measurements is discussed. This unique instrument incorporates a closed-loop control system to measure skin-friction force. The force acts tangent to the surface of a five-inch-diameter sensing element over which wind-tunnel air flows. A linear force motor exerts a restoring force which nulls the position of the sensing element. The applied skin-friction force is measured by sensing the quantity of direct current through the motor necessary to achieve null position.

A manual control mechanism varies the position of the sensing element relative to the aerodynamic surface in a direction perpendicular to air flow. Sensing element protrusion or recession is controlled and sensed remotely. Other sensing element characteristics which can be altered systematically are surface roughness, gap width, and temperature.

A dummy skin-friction balance is described which was designed and constructed to measure loads which act perpendicular to the skin-friction sensing element during tunnel starts and during flow breakdown. Results of wind-tunnel experiments conducted with the dummy balance are presented.

Also described are the skin-friction balance design criteria and the feedback control system analysis. Appendix B treats the derivation of control system equations which lead to the overall

system transfer functions and block diagrams. Finally, performance characteristics of the feedback control system are treated to ascertain that the primary design objectives are satisfied.

CHAPTER I

INTRODUCTION

The accurate prediction of skin-friction (viscous shear) drag is essential in the design of large, high speed, long range aircraft. Skin friction may contribute over one-third of the total drag (35 per cent) on a supersonic transport flying near maximum lift-to-drag ratio (ref. 1). Full-scale performance estimates for these aircraft depend on direct measurements of skin friction in wind-tunnel tests. Systematic error sources in direct skin-friction measurements are known to exist but these sources are not adequately established. Attendant errors are introduced in the measurement process by the mere presence of the measuring device since the measuring device alters physical characteristics of the aerodynamic surface. Direct skin-friction measurements are most often made with a force transducer, hereinafter referred to as a skin-friction balance. The measurement is accomplished by sensing the viscous shear force, in the flow direction, which acts tangential on the surface of a sensing element that is flush mounted with the aerodynamic surface. Figure 1 shows a sensing element flush mounted with the inside wall of a wind tunnel. The tunnel wall serves as the aerodynamic surface in tunnel boundary-layer studies.

It is the purpose of this thesis to develop a skin-friction balance for use on a tunnel wall surface. Balance design features allow intentional measurement error sources to be induced systematically. The completed instrument permits programed investigative studies of the

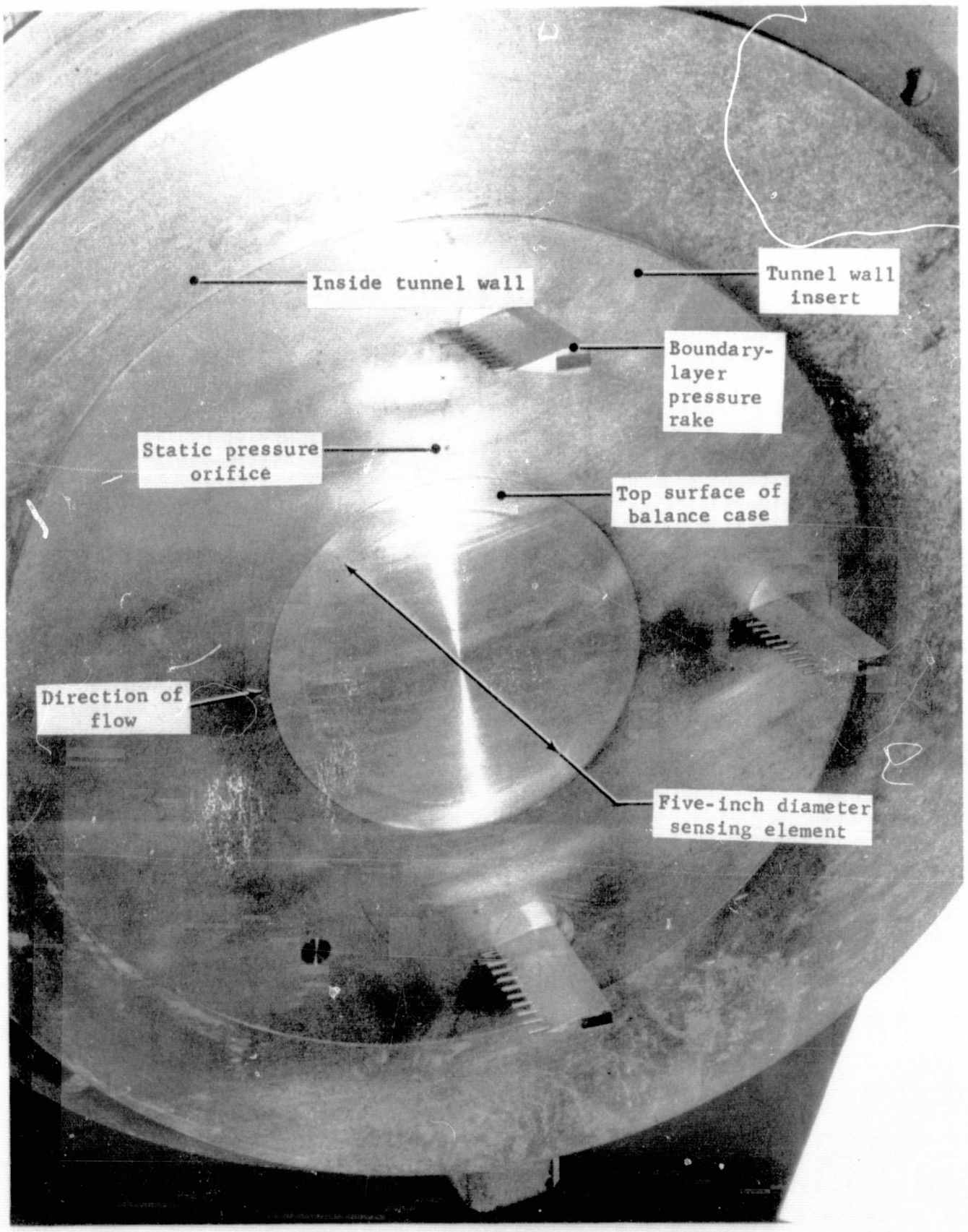

Figure 1. View from inside of wind-tunnel test section showing the dummy skin-friction balance installation.

direct skin-friction measurement technique. Surface characteristics which can be altered with this special balance are: (1) a discontinuity consisting of a clearance gap between the sensing element and the wall surface, (2) protrusion and recession of the sensing element relative to the wall surface, (3) temperature differences between the sensing element and the wall surface, and (4) surface roughness of the sensing element. Wind-tunnel experiments with this balance will relate the significance of measurement errors when one or more of the above listed error sources are present. These results are needed to aid the aerodynamicist in formulating expressions to correct other skin-friction data obtained by direct measurements, and to establish design criteria for new skin-friction balances.

The literature encompasses a variety of skin-friction measurement objectives and test conditions (refs. 2-15). Contained therein are several different schemes for making the measurement. Some work has been directed toward the investigation of errors caused by step discontinuities and temperature differences between a tunnel wall and a skin-friction sensing element (refs. 16 and 17). However, many of the skin-friction instruments reported on in the literature are of the deflection, or open loop, type. In the deflection type instrument the sensing element is spring supported and must translate in the flow direction an amount proportional to skin-friction force. A measure of the sensing element deflection is used to determine the force. In a few instances the null balance principle of operation has been or is being applied (refs. 14 and 15).

The skin-friction balance which is the subject of this thesis operates on the feedback principle. Distinct advantages of feedback control are: (1) the sensing element can maintain a given position throughout the load range, (2) component variations due to age and/or temperature have less influence on balance sensitivity changes, and (3) the sensing element suspension can be made sufficiently stiff to safely withstand excessive dynamic and static loads without adversely reducing sensitivity. Information contained in this thesis is applicable to new force and pressure transducer designs. This balance design incorporates features which will insure wide versatility in varying sensing element characteristics to study direct skin-friction measurement errors.

CHAPTER II

BALANCE REQUIREMENTS

The subject skin-friction balance is designed to operate in accordance with certain performance goals. An unknown requirement was the perpendicular loads which the sensing element and its suspension must withstand during tunnel starts and flow breakdown. Therefore, it was necessary to determine tunnel starting and flow breakdown loads experimentally with the use of a special force transducer.

The dummy skin-friction balance. A special force transducer, presented in Figure 2, was designed and constructed to measure perpendicular loads which act on the skin-friction sensing element. This special transducer is hereinafter referred to as the Dummy Skin-Friction Balance (DSFB). A five-inch-diameter sensing element is suspended from a strain-gage load cell which is located internal to the DSFB as shown in Figure 3. The load cell, presented in Figure 4, has a load capacity of one thousand pounds and a spring constant of 1×10^6 lb/in. With this load cell the DSFB has a 2.3 KHz resonant frequency and a damping ratio of 7×10^{-3}. Presented in Figure 5 is the DSFB calibration curve.

Wind-tunnel experience with the DSFB. Perpendicular loads on the sensing element were measured in the NASA-Langley twenty-inch variable supersonic tunnel. The twenty-inch VST facility is a blowdown tunnel having a stagnation pressure range of twenty-five to one hundred thirty psia. This tunnel exerts the most severe starting and flow

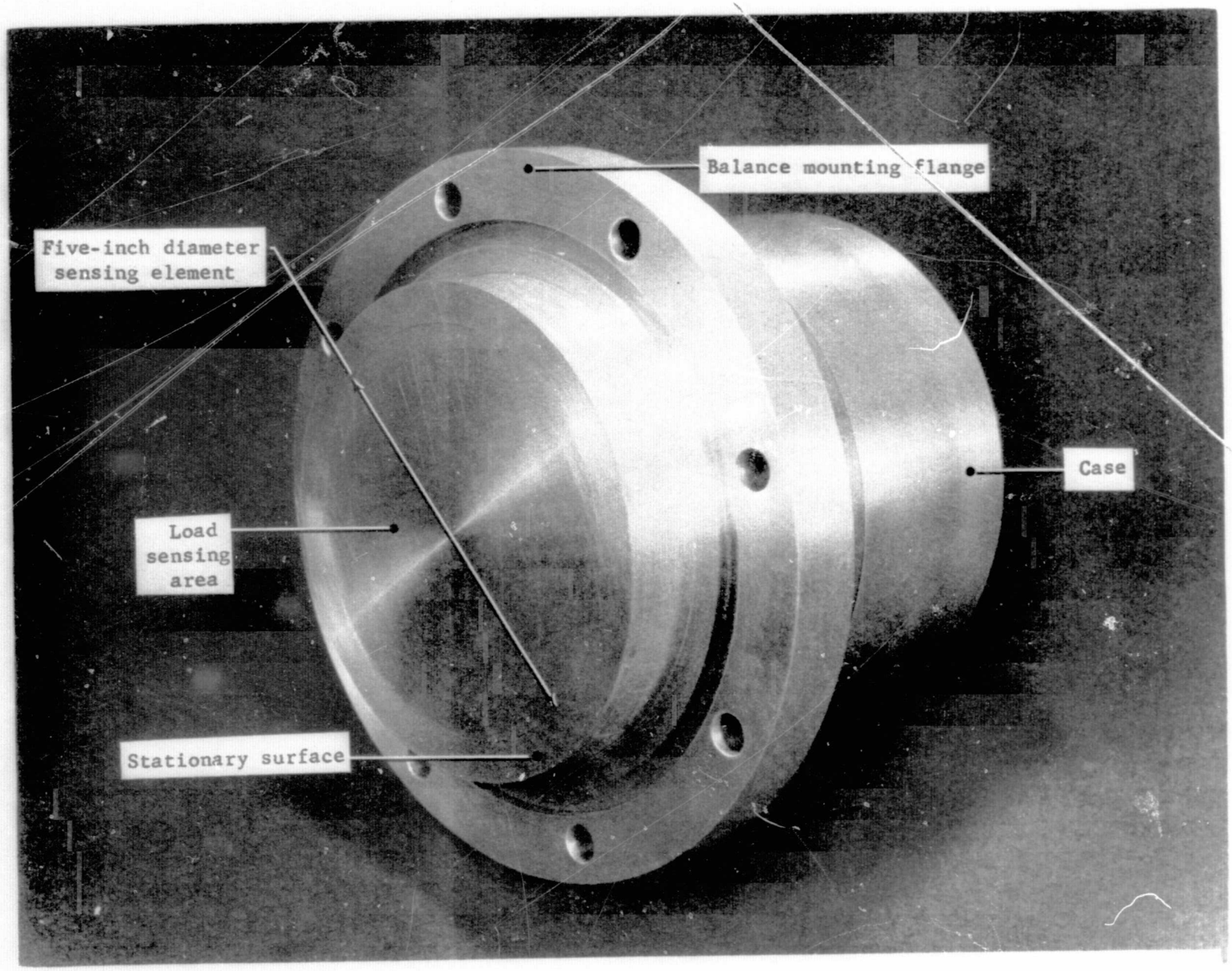

Figure 2. Dummy skin-friction balance.

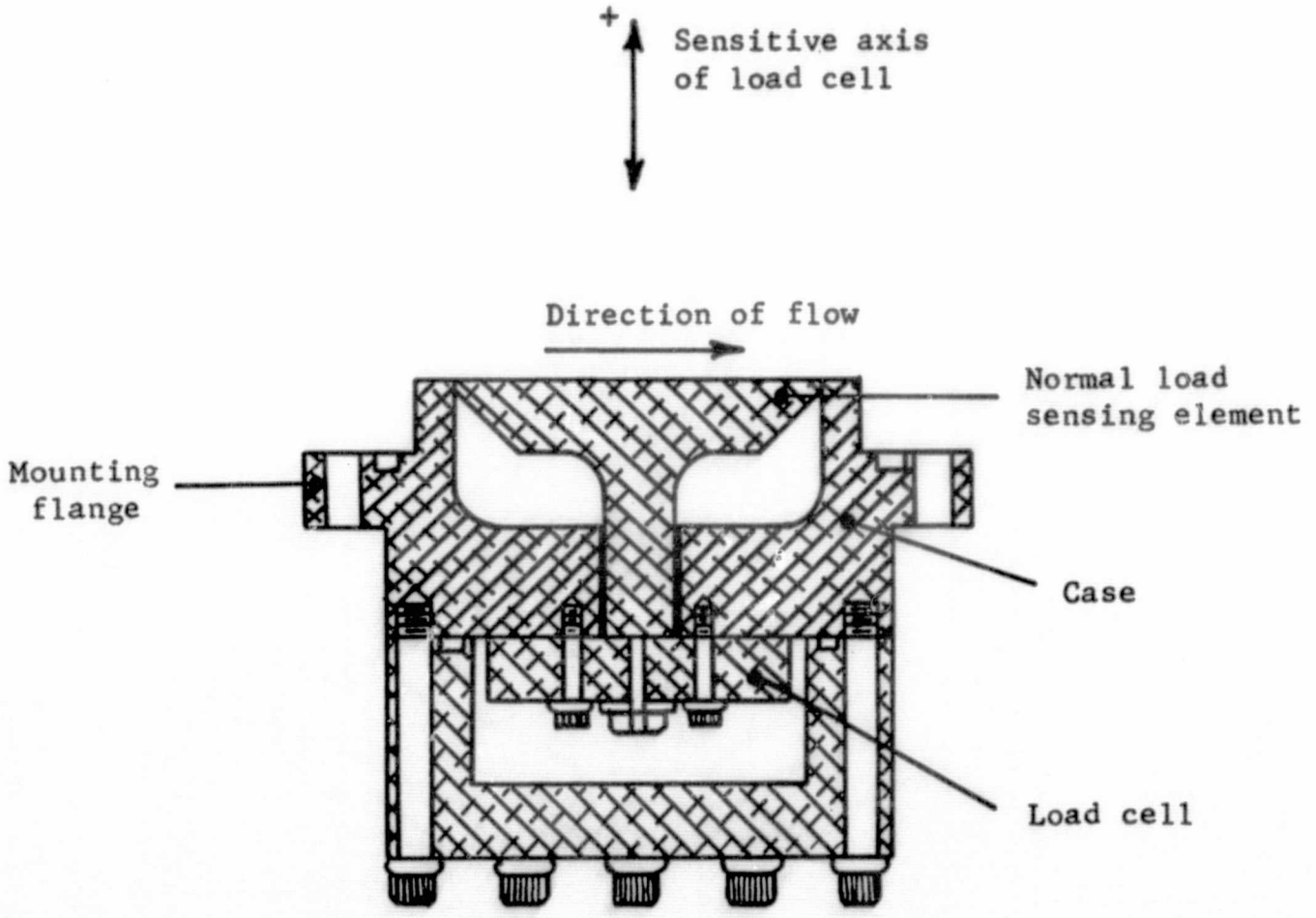

Figure 3. Cross section drawing of the dummy skin-friction balance.

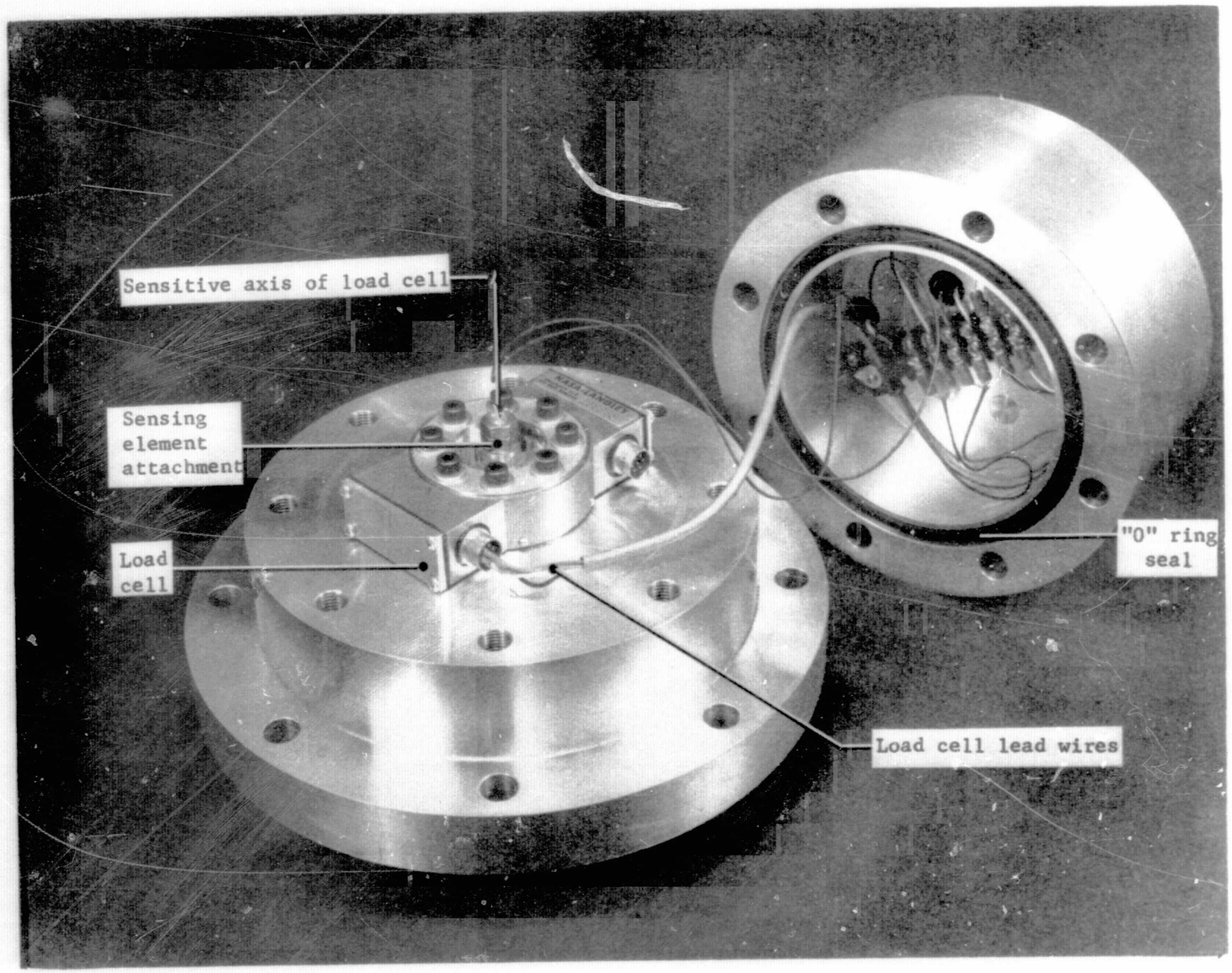

Figure 4. Disassembled dummy skin-friction balance.

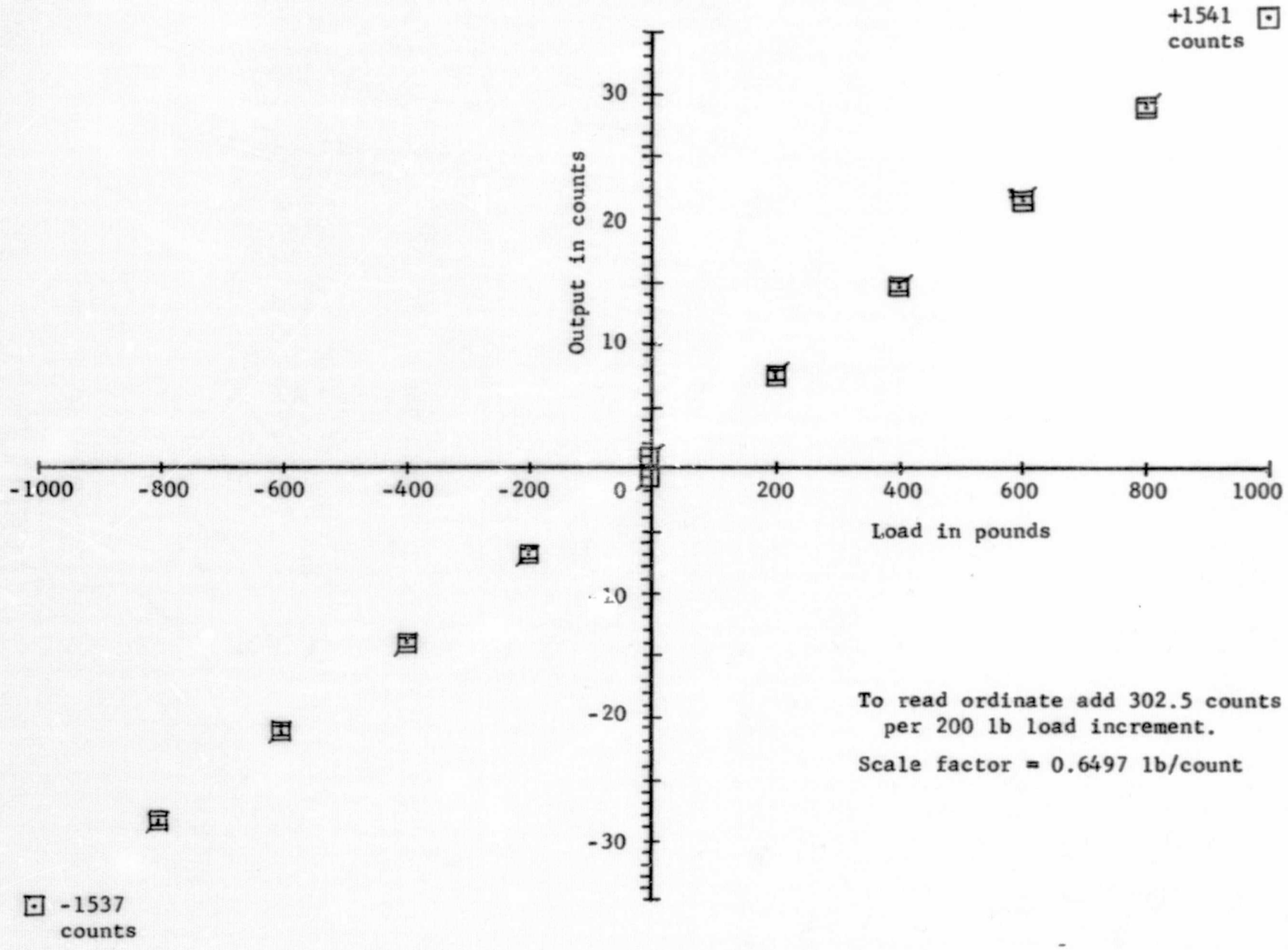

Figure 5. Load cell calibration curve.

breakdown loads of all the tunnels in which the subject skin-friction balance will be used. Presented earlier in Figure 1 was the DSFB installed on the side wall of the twenty-inch VST facility. Figures 6(a) and 6(b) show force data obtained in a series of tests in the VST facility. During tunnel starts, the maximum measured normal load was one hundred eighteen pounds directed outward from the tunnel. During flow breakdown, the maximum load was one hundred sixty-two pounds in the same direction. As a result of these tests, the sensing element suspension in the subject skin-friction balance is designed to safely withstand static normal loads of five hundred fifty pounds.

Skin-friction balance design specifications. Additional skin-friction balance design specifications are listed below:

Skin-friction range	0.25×10^{-2} psi to 0.25×10^{-1} psi
Force range	5×10^{-2} lb to 5×10^{-1} lb
Sensing element diameter	5 in.
Sensing element temperature range	70° F to 200° F
Sensing element surface finish	20 to 35 μin. RMS
Maximum sensing element protrusion	1/16 in.
Maximum sensing element recession	1/16 in.
Gap width range	5×10^{-3} in. to 5×10^{-2} in.
Test time	1 to 5 minutes
Full-scale output	100 mV ± 10 mV
Output impedance	100 ohms or less
Temperature operating range	70° F to 80° F
Combined error	Not greater than 1 per cent of full scale

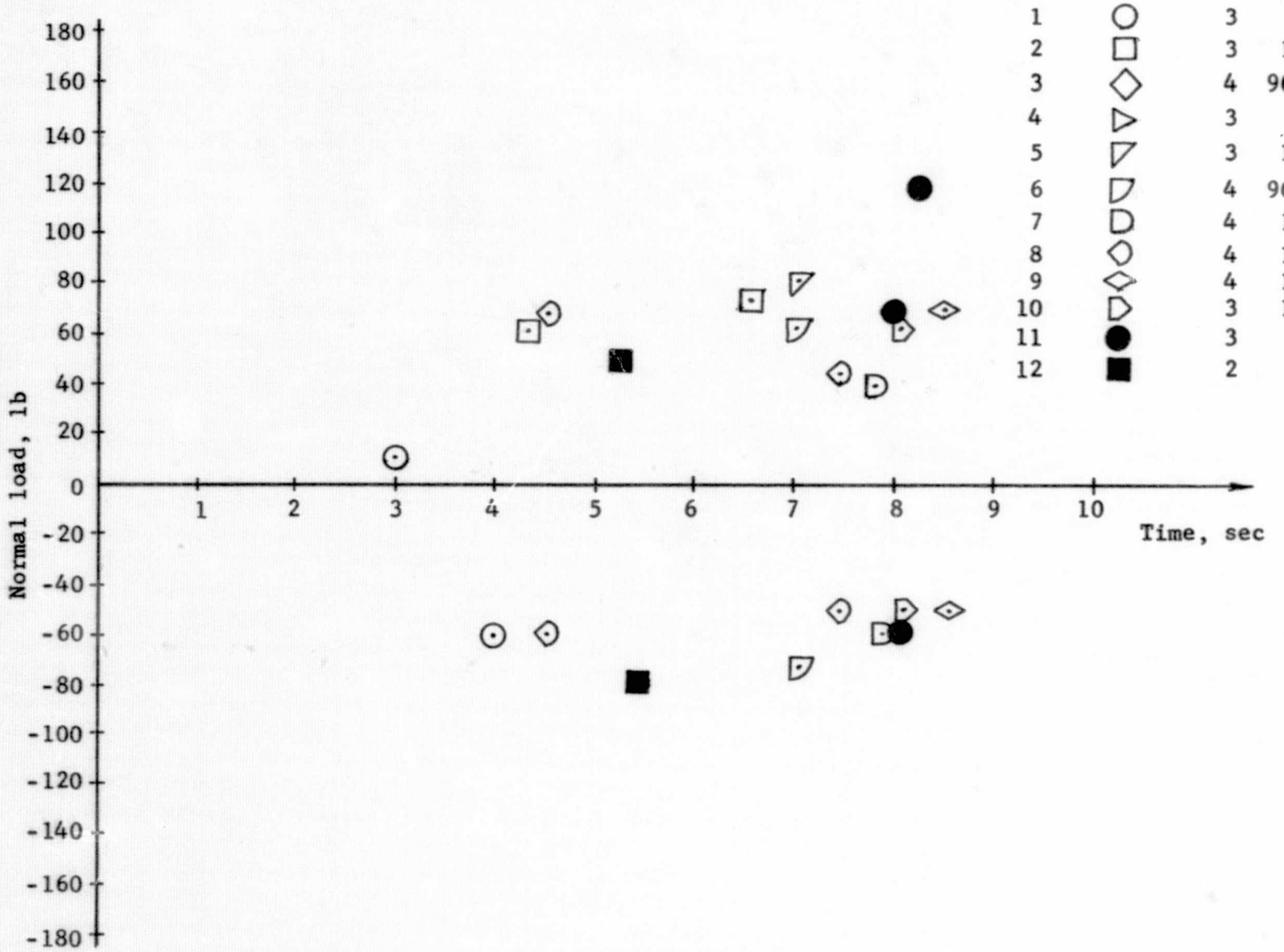

Test no.	Symbol	Mach no.	P_t	T_t
1	○	3	56	70
2	□	3	112	115
3	◇	4	96.5	129
4	△	3	56	121
5	▽	3	112	115
6	▷	4	96.5	129
7	▷	4	110	129
8	◇	4	110	130
9	◇	4	110	129
10	▷	3	112	121
11	●	3	56	121
12	■	2	66	108

Figure 6(a). Normal load on DSFB versus time after initiation of tunnel start.

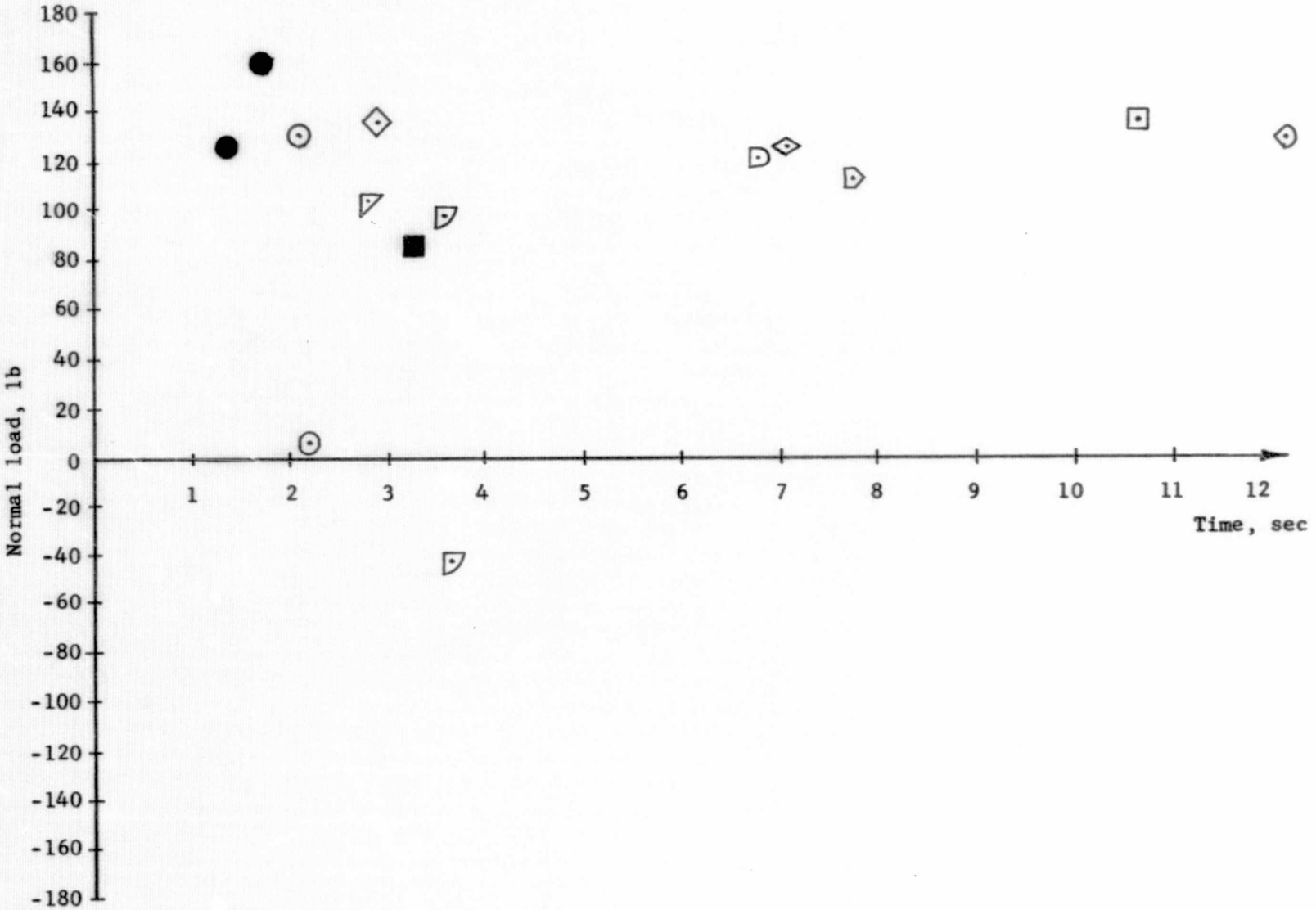

Figure 6(b). Normal load on DSFB versus time after initiation of tunnel shutdown.

Additional design features of the subject balance are: (1) internal calibration capability, (2) interchangeable sensing elements, (3) counterbalanced arm, and (4) remote control and sensing of measuring element protrusion and recession.

In practice, the measurand (skin friction) will act on the balance as a terminated ramp with the steady-state portion of the input acting from one to five minutes. Thus, the nature of the input and the test duration do not impose rigid response requirements on the balance. However, associated with most wind tunnels are rotating machinery and wind noises which impose a vibrational environment. The balance must attenuate disturbances introduced by these sources.

The balance design project undertaken in this thesis is based upon satisfying the measurement requirements discussed in the present chapter.

CHAPTER III

BALANCE DESIGN

The advantages of feedback control as discussed in Chapter I influenced the decision to design a closed-loop control balance. An additional benefit, from an operational standpoint, is realized with a type "one" servomechanism (one integration in the open-loop transfer function) (ref. 18). Under a steady-state load the type one system will operate with zero displacement after transients have disappeared. This design feature is used since it reduces the width of the required gap. In addition, a constant gap configuration is maintained while the sensing element is loaded. A changing gap would otherwise introduce an unwanted variable in the measurement process.

The skin-friction balance is composed of both electrical and mechanical components. Presented in Figure 7 is an assembly drawing of the balance. This drawing illustrates the physical relationship between the various parts of the balance. A balance arm is used to sum forces in the control system. The balance arm is attached to the frame with two flexure pivots. Installed on the top end of the balance arm is the skin-friction sensing element. Attached to the opposite end of the arm are two electromagnetic linear force motor magnets. One of the motors is used to exert the restoring load on the balance arm. The other motor is used to exert a secondary calibration load on the balance arm and as a tachometer for damping. Balance arm end position along the flow axis is sensed with a linear variable differential transformer

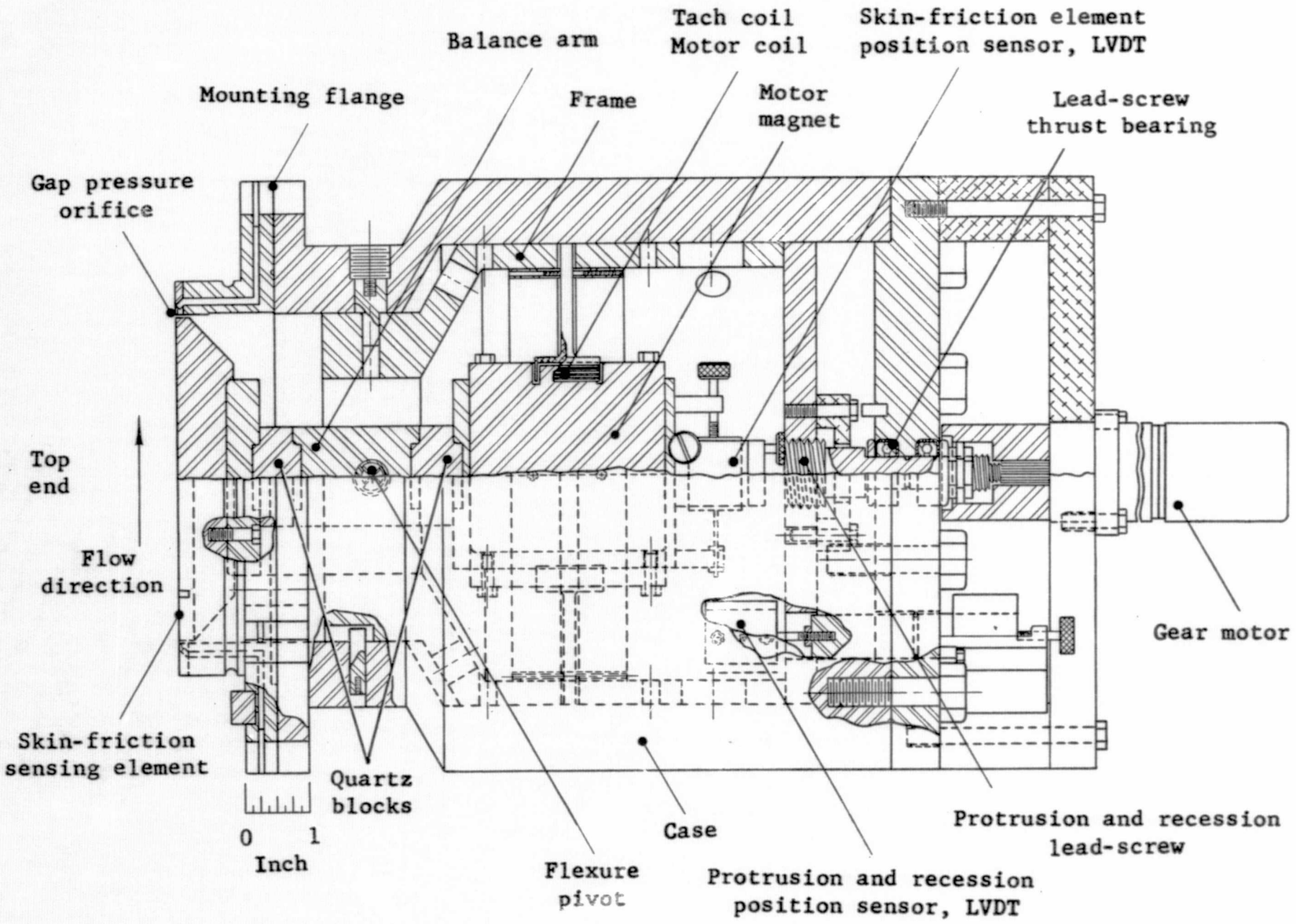

Figure 7. Cutaway assembly drawing of the skin-friction balance.

(LVDT). The control system error signal is derived from this LVDT. A second LVDT is used, independent of the control system, to measure protrusion or recession of the sensing element relative to the tunnel wall surface. This design feature provides means to establish a relationship between apparent skin-friction force and sensing element misalinement.

The tangential force which acts on the sensing element in the flow direction is determined by sensing the quantity of electric current in the motor coil which is required to accomplish null position. A measure of the subsequent voltage drop in the motor coil circuit serves as the output voltage.

An operational dc power amplifier provides current to the restoring force motor. An operational voltage amplifier provides integral-plus-proportional control. This amplifier introduces the integration relative to arm displacement necessary to realize a type one system. A second voltage amplifier is used to amplify the tachometer signal. The amplified tachometer signal introduces equivalent damping in the control system.

Intentional protrusion or recession of the sensing element is accomplished with a gearmotor driven lead-screw mechanism. The lead-screw is supported on thrust bearings which are located in the bottom cover plate.

A five-inch-diameter skin-friction sensing element was selected on the basis of magnifying the skin-friction load. Local skin friction is a low magnitude viscous shear phenomenon. As the measurand,

skin-friction magnitude varies directly with sensing element area in a given flow (ref. 19). In upcoming wind-tunnel tests where this balance will be used, the maximum skin-friction load is expected to be not more than 0.5 pound on a five-inch-diameter sensing element. The measurement of this load under tunnel conditions with as little as one per cent error is considered feasible.

Two extraneous loads are usually associated with skin-friction measurements. These loads are pressure drag and buoyant force. Pressure drag acts on the sensing element whenever the element protrudes into the flow stream. For a given protrusion height, the ratio of pressure drag-to-skin friction drag is lessened as the sensing element diameter increases. This drag ratio is proportional to h/d, where h is the protrusion height and d is the sensing element diameter. The incorporated design feature of variable sensing element protrusion height and recession permits the investigation and formulation of protrusion and recession effects.

A buoyant force is registered by the balance when the sensing element is situated in a static pressure gradient along the flow direction. The buoyant force exists by virtue of the difference in pressure between the leading and trailing edges of the sensing element. To facilitate the measurement of such a pressure gradient, six miniature pressure orifices are located around the periphery of the gap. The buoyant force is computed from pressure data and is used to correct recorded skin-friction data.

Five interchangeable skin-friction sensing elements permit systematic changes in element characteristics including surface roughness, gap width, and edge configuration. These elements can be altered or new elements constructed to realize additional variations in element characteristics.

All joints in the balance are sealed with "O" rings to preclude air leakage. During tunnel tests the balance case interior operates at the tunnel static pressure level. The balance case exterior operates at atmospheric pressure. Air leakage through the balance case would introduce unwanted flow disturbances in the gap between the sensing element edge and the adjacent surface.

Structural parts of the balance are made of free machining Invar alloy. Invar has a thermal expansion coefficient of only 0.7×10^{-6} in./in./^{o}F over the temperature range of zero to two hundred degrees Fahrenheit. This material was selected on the basis of low thermal expansion and good dimensional stability. These qualities also enhanced machining and fitting of parts with close tolerances. Additional physical properties of Invar are found in the literature (ref. 20).

Further discussion of the mechanical and electrical components which compose the balance follows.

1. MECHANICAL COMPONENTS

Skin-friction sensing elements. The balance accommodates skin-friction sensing elements up to five inches in diameter. The diameter

of five existing sensing elements differs only slightly to realize gap widths from 5×10^{-3} inch to 5×10^{-2} inch. The sensing elements are also constructed of Invar and have a maximum thickness of one inch. A recessed circular flat on the bottom of each element provides an ASA class four fit with the balance arm to realize concentric alinement. A bolted joint between the element and arm permits quick interchangeability of elements. The top surface of the sensing elements is circular ground to the required finish.

The balance arm. The balance arm supports the skin-friction sensing element on the top end and the two motor magnets on the opposite end, as previously mentioned. Equal arm lengths of three inches are used between the pivot axis and lines of action of skin-friction force and motor force. This arrangement yields a one-to-one correspondence between the two forces at the null condition.

Fused quartz sections installed in the arm on each side of the pivot axis serve as thermal insulators (see Appendix A). Thermal insulation is required to reduce heat conduction from the sensing element to other parts of the balance. The quartz sections also disrupt the magnetic flux line path from the motor magnets to the skin-friction sensing element.

The flexure pivot. The balance arm is supported by a flexure pivot which permits angular rotation of the arm and resists forces which act on the arm. The pivot is composed of two Bendix 'Free Flex' pivots (ref. 21). These pivots are made of stainless steel and consist

of a two element cross flexure mounted in a one-half inch diameter case. This design permits nearly frictionless angular motion of the balance arm. However, in the closed-loop control system only pending angular motion of the arm is encountered under static load conditions. The torsional spring constant of the flexure pivot is one hundred four lb-in./radian.

The balance frame. The balance frame supports the balance arm and makes a close sliding fit with the balance case. The flexure pivot discussed above provides a mechanical connection between the balance arm and the case. Sliding motion of the frame relative to the case imparts translation to the sensing element which induces sensing element recession or protrusion. Rotation of the frame inside of the case is prevented through the use of a key and keyway in the respective parts.

The lead-screw mechanism. A gearmotor driven lead-screw is used to systematically translate the balance frame relative to the balance case along the common longitudinal axis. The screw mechanism translates the frame at a rate of one-sixteenth inch per minute or less to achieve any desired protrusion or recession up to one-sixteenth inch.

The balance case. The balance case contains internally the frame, balance arm, motors, tachometer, lead-screw, and position sensors. A circular flange at the top end of the case is used to attach the case to the wind-tunnel wall. The top separable half of

the case flange contains pressure orifices for monitoring static pressure in the sensing element gap.

Gap pressure orifices. Six pressure orifices are used to measure the static pressure in the gap between the sensing element and the adjacent stationary wall. The pressure orifices are installed in separate metal blocks which measure 0.010 inch wide by 0.125 inch high by 0.500 inch long. Figure 8 presents a plan view of a single pressure orifice block. Figure 9 presents a size comparison of one pressure orifice and a human hair. The orifice blocks are inserted and bonded into machined slots in the case flange. The orifices range in size from one mil to two mils diameter and are located within five mils of the aerodynamic surface. Damaged or plugged orifices may be readily removed and replaced with another orifice block which contains an orifice.

2. ELECTRICAL COMPONENTS

Linear force motors. Two linear force motors with permanent magnet poles are used to exert electromagnetic forces on the balance arm. One of these motors is used in the servocontrol system to exert balance arm restoring loads. The other motor is used as a tachometer for damping and to exert a secondary calibration load on the balance arm. The magnet pole pieces are attached to the lower end of the balance arm. The motor coils extend inside of the magnets and are firmly attached to the balance frame. Thus, no direct physical contact

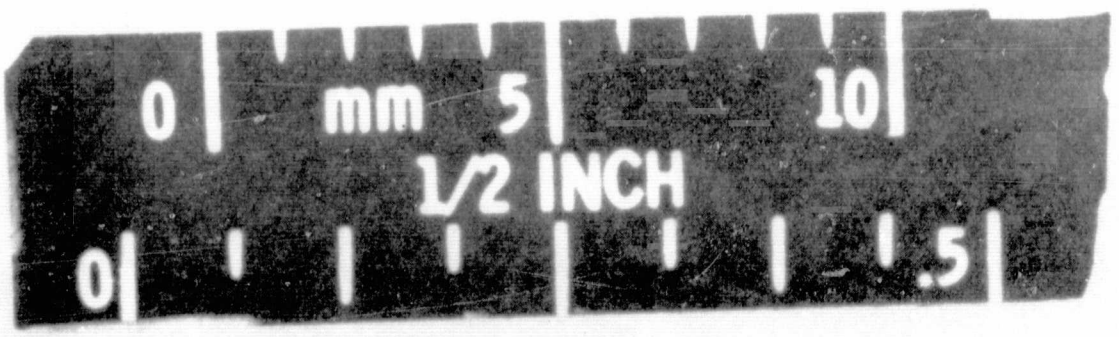

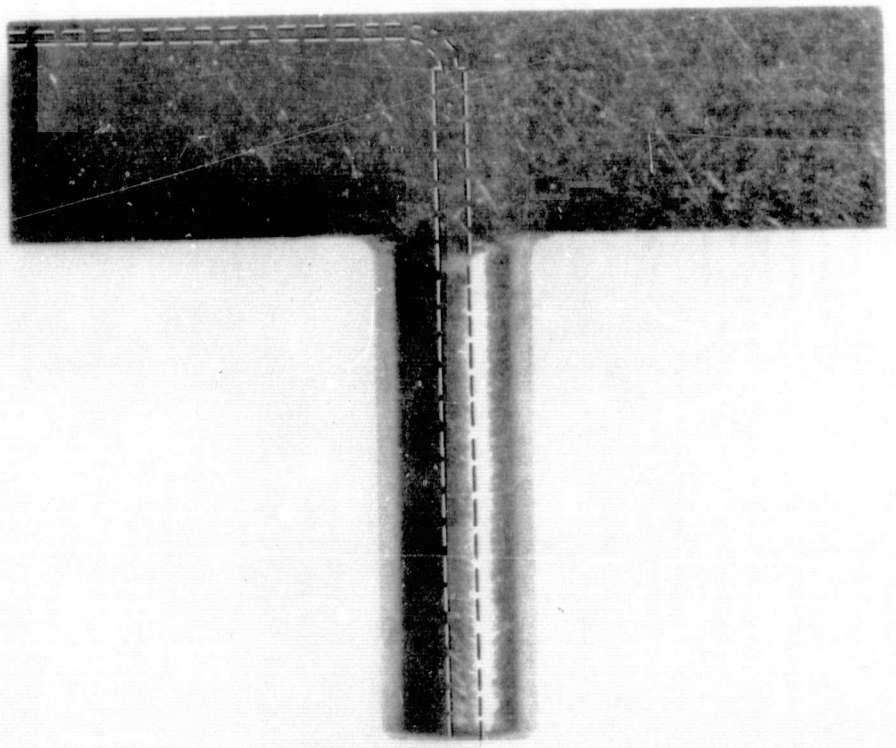

Figure 8. Magnified plan view of pressure orifice block.

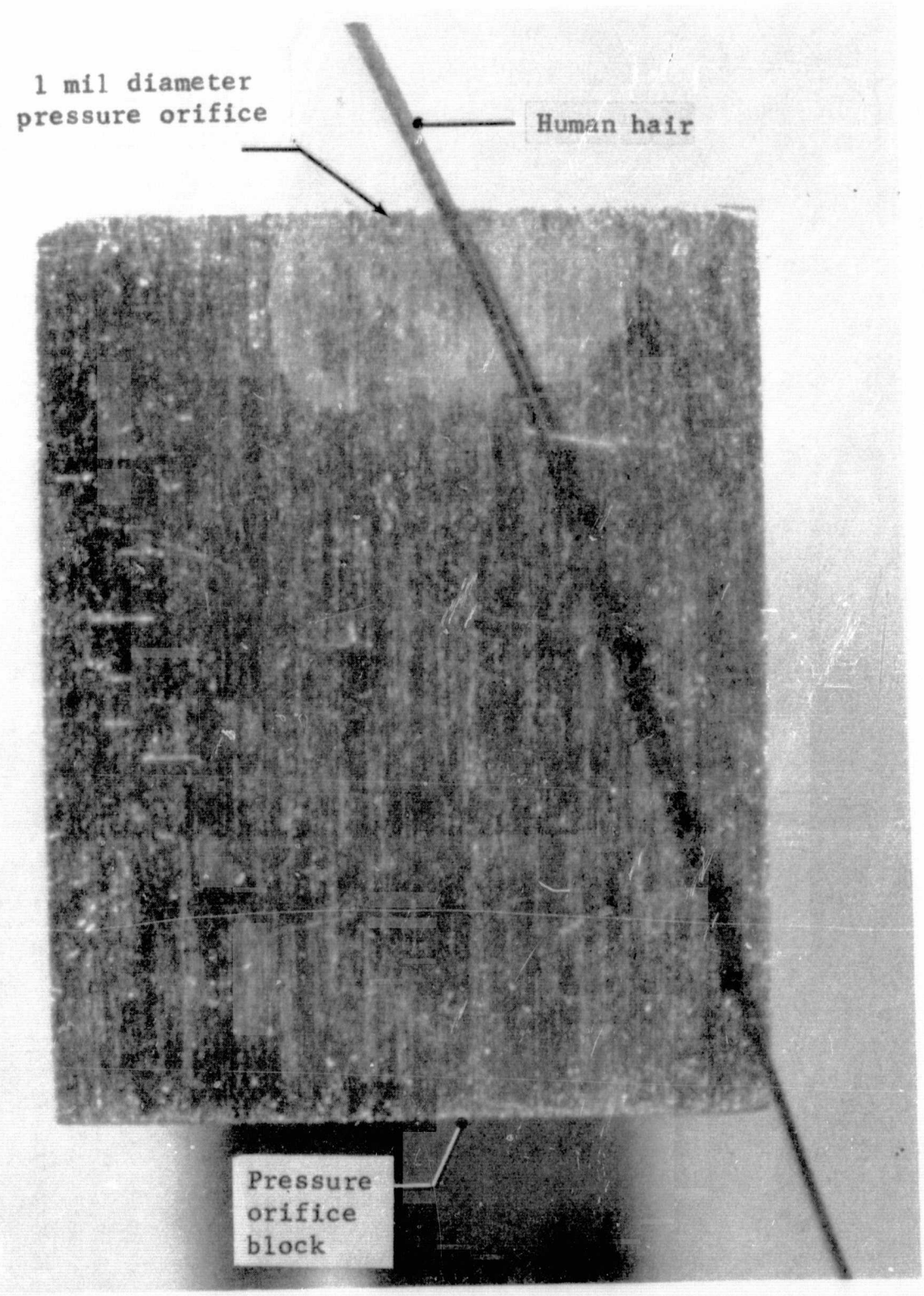

Figure 9. Magnified view of pressure orifice.

is made between the coils and the magnets. This arrangement precludes the need of transferring electrical power to the balance arm. Experience relates that power leads in parallel with a low force measuring system usually results in operational difficulties such as zero shifts, hysteresis, and nonrepeatability.

Displacement transducers. Use is made of two linear variable differential transformers (LVDT) to sense displacement. A LVDT gives an output voltage proportional to displacement by sensing the inductive coupling between primary and secondary transformer windings (ref. 22). One LVDT provides the error signal in the feedback system. A second LVDT senses the amount of sensing element protrusion or recession. This second LVDT is not an element in the servo system.

The servo amplifier. The servo amplifier supplies up to plus or minus one ampere of direct current to the repositioning motor. This amplifier is a solid state operational type with differential input. Amplifier output impedance is ten ohms. The balance output voltage is obtained from the voltage drop across a fixed resistor placed in series with the motor coil.

The integral-plus-proportional control amplifier. This voltage amplifier contributes integral-plus-proportional control in the servo system. The integration required to realize a type one servo mechanism is provided by this amplifier. Control action of the integral-plus-proportional control amplifier is with respect to the balance arm displacement along the flow axis.

The tachometer amplifier. The tachometer amplifier enlarges the tachometer output signal to provide damping in the control system. Equivalent damping may be changed by altering the gain of this amplifier.

The thermocouple. An iron-constantan thermocouple attached to the sensing element measures sensing element temperature. In some tests the sensing element will be elevated in temperature in the range of seventy to two hundred degrees Fahrenheit.

All amplifiers and power supplies are located external of the balance proper and are hard wired to the components which are located internal to the balance case.

Table I lists the components discussed above. Where applicable, the source and scale factor for each component are listed.

TABLE I

LIST OF COMPONENTS

Component	Manufacturer	Model no.	Scale factor
LVDT position sensor	Schaevitz Engineering	050 dc	90.4 $\frac{\text{volts}}{\text{inch}}$
Force motor and tachometer	Agac-Derritron Inc.	VP.2	0.85 $\frac{\text{lb}}{\text{amp}}$
Gearmotor	Globe Industries Inc.	102A193-10	100 $\frac{\text{lb-in.}}{\text{amp}}$
Servo amplifier	Airpax Electronics	AMS24	1 amp at ±10 V
Integrating amplifier and tachometer amplifier	Fairchild Semiconductor	A00-4	7 mA at ±10 V
Thrust bearing	Boston Gear	603$\frac{1}{4}$	NA
Flexure pivot	The Bendix Corporation	5016-400	104 $\frac{\text{lb-in.}}{\text{radian}}$
Lead-screw	NA	NA	$\frac{1}{2}$ - 12 UNC
Thermocouple	Leeds and Northrup Company	NA	0.05 mV/°C

CHAPTER IV

FEEDBACK CONTROL SYSTEM ANALYSIS

Conventional methods of analysis are used to develop the transfer functions and block diagram for the balance control system. An integrator is used in the feedback path to realize a type one system and a tachometer provides equivalent damping. Type one control action is necessary to produce zero displacement of the sensing element under static load conditions. Control system equations used in the analysis are derived in Appendix B. Force motor inductance and back emf are small and are therefore considered negligible. The diagram of Figure 10 relates the quantities of force, length, and angle with relation to the balance arm.

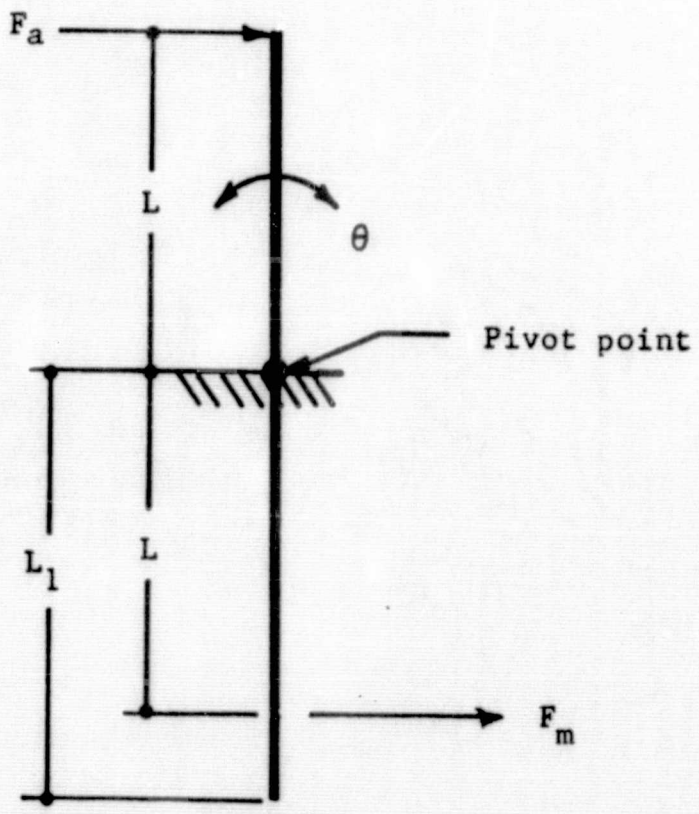

Figure 10. Diagram of balance arm.

Control system block diagrams. Presented in Figure 11 is the unsimplified block diagram of the balance control system. A simplified block representation with E_r equal to zero is presented in Figure 12. A reference voltage other than zero would introduce an offset in sensing element position. To investigate sensing element position as a function of input force, the diagrams of Figures 13(a) and 13(b) were constructed. Steady-state position of the sensing element in response to a step force input is examined by use of the final value theorem and the closed-loop transfer function. Referring to the block diagram in Figure 13(b), the closed-loop transfer function is

$$\frac{\theta(s)}{F(s)} = \frac{G}{1 + GH} = f_1(s) \tag{1}$$

The final value theorem applied to the closed-loop transfer function gives the steady-state angular displacement of the balance arm when the balance is subjected to a step force input as

$$\lim_{t \to \infty} \theta(t) = \lim_{s \to 0} \frac{s|F_a(s)|}{s} f_1(s) = 0 \tag{2}$$

As a consequence of zero arm displacement given by equation (2), the integrator serves its intended purpose. Zero arm displacement also implies that the motor force is equal to the applied force since the arm lengths are equal. Any discrepancy in the force equality by virtue of unequal arm lengths is accounted for in the balance calibration.

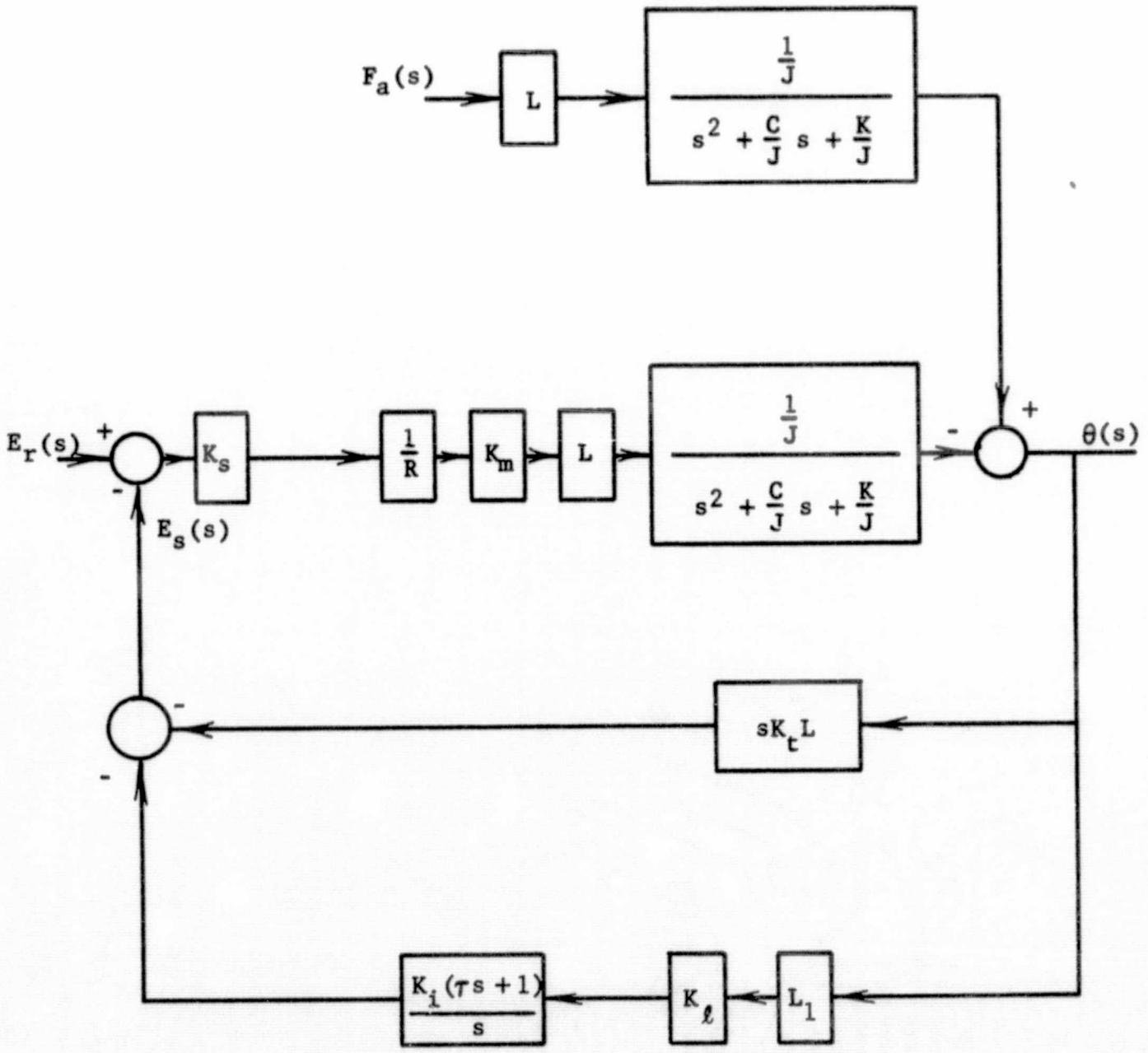

Figure 11. Unsimplified block diagram for skin-friction balance control system.

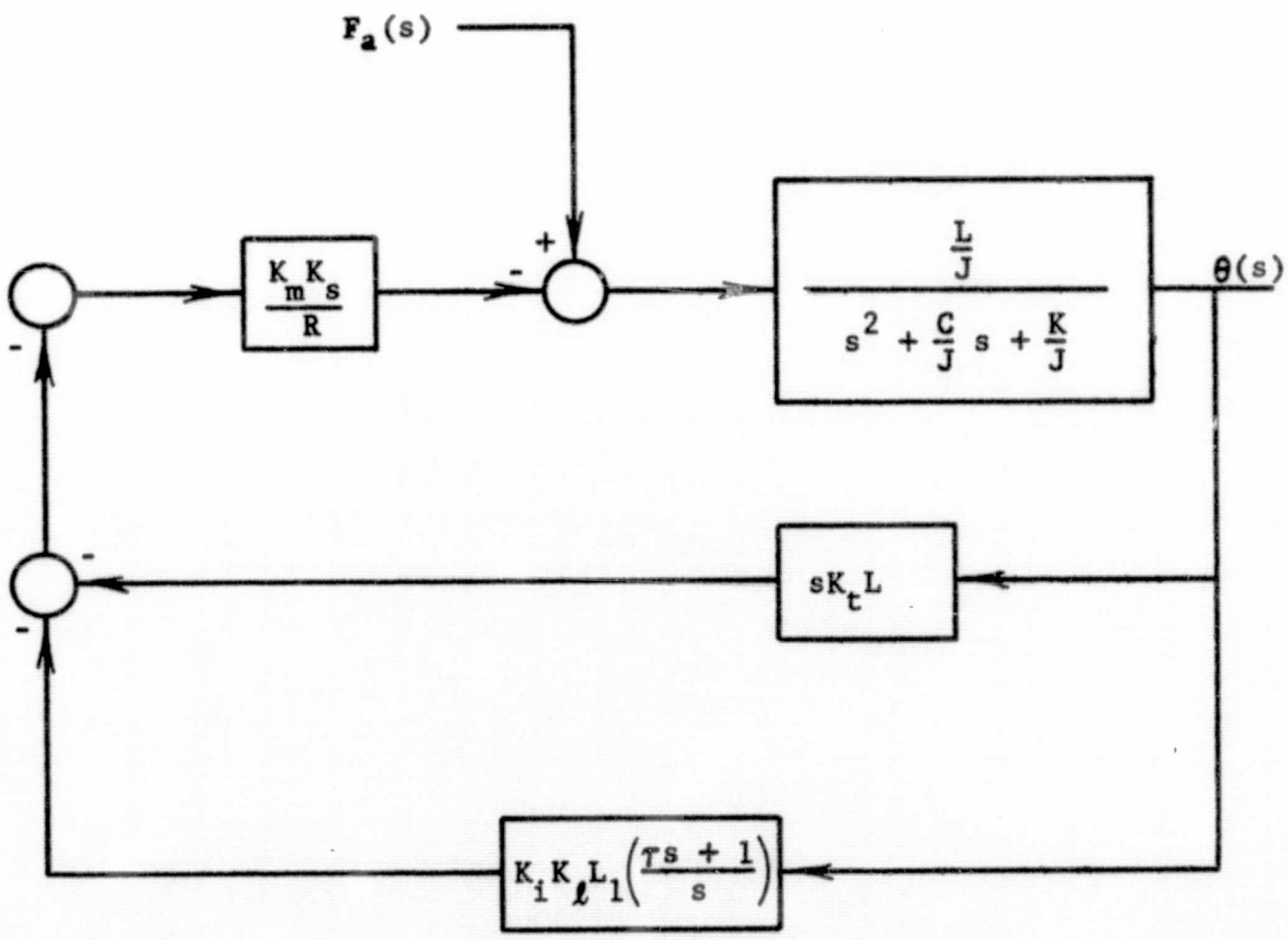

Figure 12. First simplified block diagram of skin-friction balance control system, $E_r = 0$.

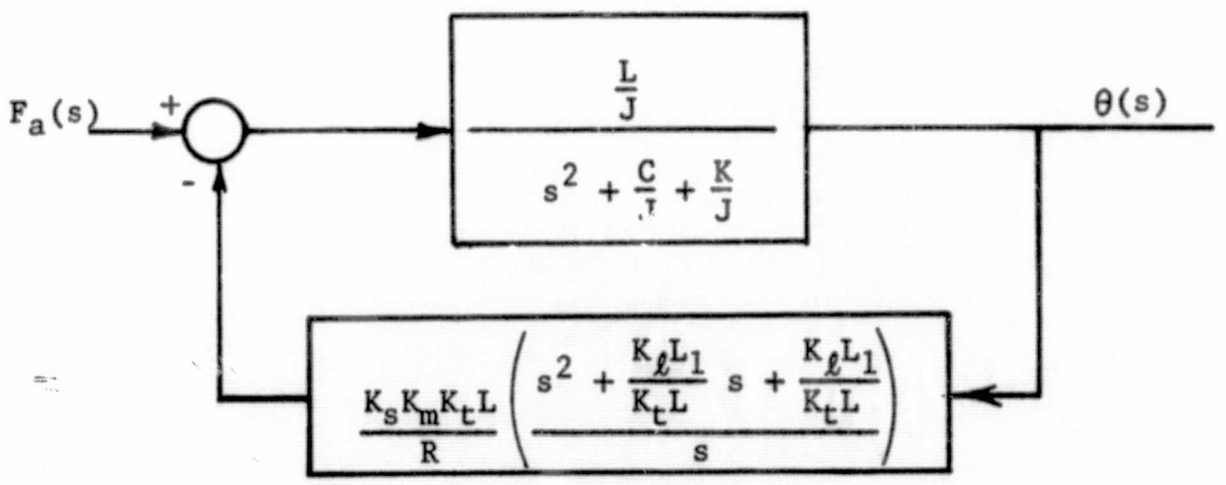

(a)

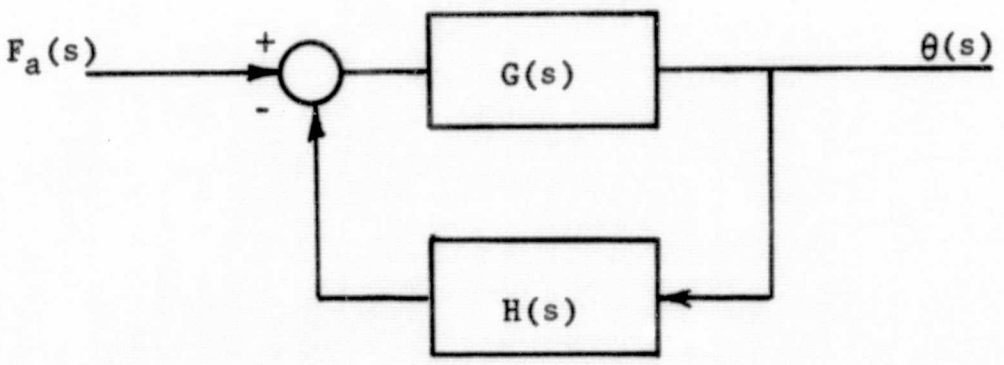

(b)

Figure 13. Block diagrams for skin-friction balance control system: (a) single block representation for forward and feedback paths; (b) letter designations for single blocks.

Another block diagram representation of the control system is presented in Figure 14. Block A of Figure 14 represents the loop gain, G times H. Minus one times the loop gain is the positive loop gain function which is represented by

$$A(s) = \frac{K_m K_s K_t L^2}{JR}\left[\frac{s^2 + \frac{K_i K_\ell L_1 \tau}{K_t L}\, s + \frac{K_i K_\ell L_1}{K_t L}}{s\left(s^2 + \frac{C}{J}\, s + \frac{K}{J}\right)}\right] \qquad (3)$$

The factor $\frac{1}{s}$ in equation (3) reveals that this is a type one system which is open circuit unstable due to the pole at the origin on the s plane.

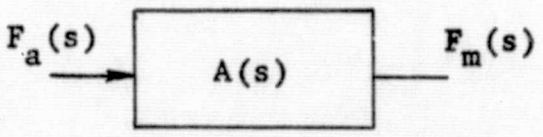

Figure 14. Block representation for balance loop gain function.

The closed-loop transfer function. The closed-loop transfer function is expressed again as

$$\frac{\theta(s)}{F_a(s)} = \frac{G}{1 + GH} \qquad (4)$$

From Figure 13(a) the closed-loop transfer function is rewritten in the form

$$\frac{\theta(s)}{F_a(s)} = \left[\frac{\frac{sL}{J}}{s^3 + \left(\frac{C}{J} + \frac{K_m K_s K_t L^2}{JR}\right)s^2 + \left(\frac{K}{J} + \frac{LK_i K_m K_s K_\ell L_1 \tau}{JR}\right)s + \frac{LK_i K_m K_s K_\ell L_1}{JR}} \right] \quad (5)$$

The characteristic equation. The system characteristic equation is represented by the denominator of equation (5) equated to zero and is written below as

$$s^3 + \left(\frac{C}{J} + \frac{K_m K_s K_t L^2}{JR}\right)s^2 + \left(\frac{K}{J} + \frac{LK_i K_m K_s K_\ell L_1 \tau}{JR}\right)s + \frac{LK_i K_m K_s K_\ell L_1}{JR} = 0 \quad (6)$$

Control system physical constants. The constant terms in equation (6) are fixed by the physical components used in the system. Three exceptions are the servo amplifier gain K_s, the integrator gain K_i, and the tachometer gain K_t which can be varied at will. Values of these terms are as follows:

$$J = 0.32$$

$$C = 4 \times 10^{-2}$$

$$K = 104$$

$$K_i = 1$$

$$K_\ell = 90.40$$

$$K_m = 0.85$$

$K_s = 10$

$K_t = 8.9$

$K_v = 9 \times 10^{-2}$

$L = 3.00$

$L_1 = 5.31$

With K_s equal to ten, Routh's criterion established that the system is stable when $K_t > 0.032$ (ref. 18).

The loop gain function in time constant form. With the value of K_t equal to 8.9, the time constant form of the loop gain function is

$$GH = 11.84\left[\frac{(s + 1)\left(\frac{s}{18} + 1\right)}{s\left(\frac{s}{0.06 + j18} + 1\right)\left(\frac{s}{0.06 - j18} + 1\right)}\right] \qquad (7)$$

Substituting $j\omega$ for s in the loop gain function, values for the Nyquist and Bode diagrams are obtained.

The Nyquist diagram. Presented in Figure 15 is the Nyquist diagram for the control system. Crossover occurs at two hundred fifteen radians per second and at a phase angle of minus ninety-four degrees. The tachometer introduces enough lead at crossover to give the system a high degree of relative stability. The ninety-four degrees phase lag results in a phase margin of eighty-six degrees.

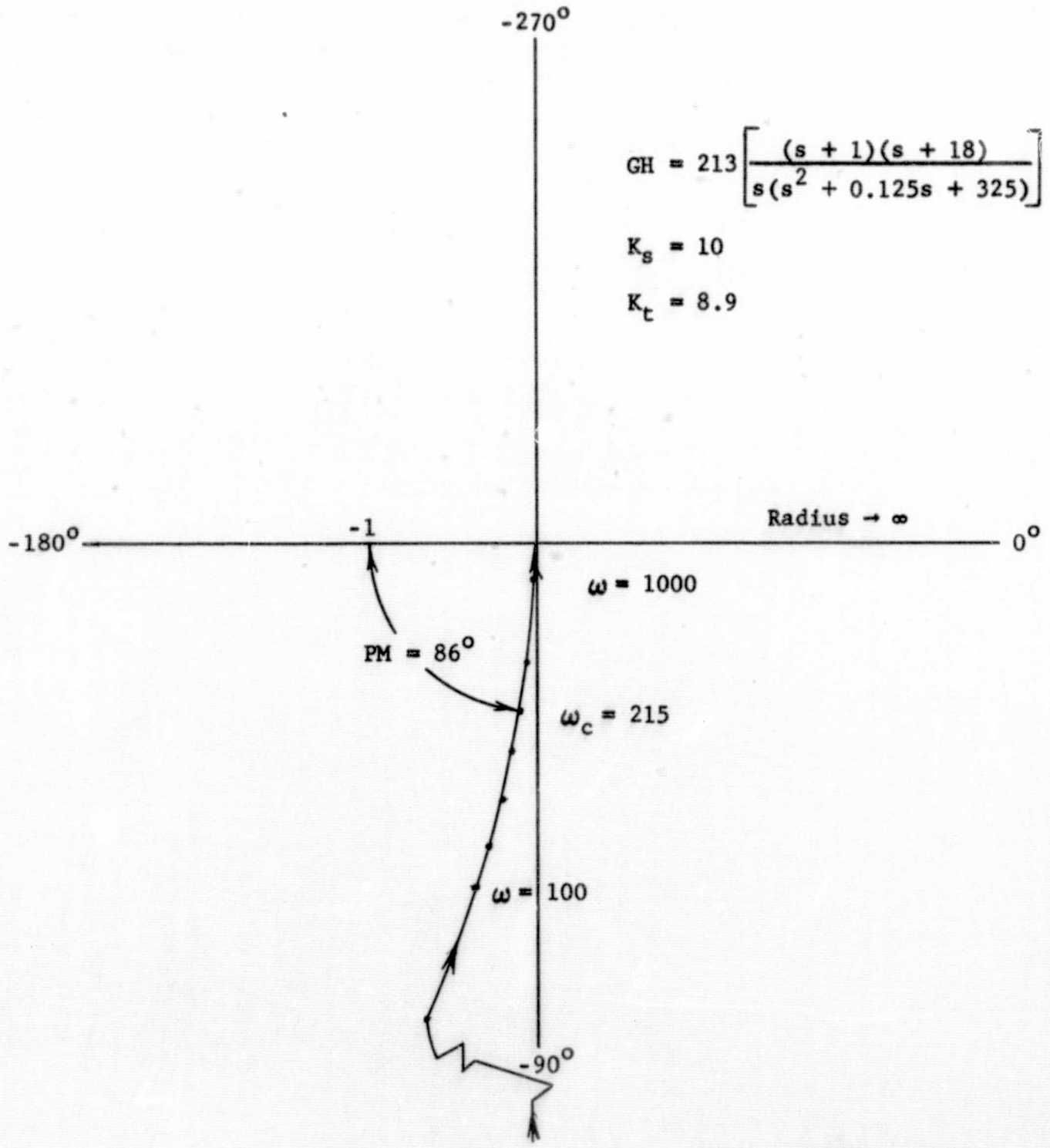

Figure 15. Nyquist diagram for the balance control system in the vicinity of crossover.

The Nyquist plot does not encircle or pass close to the critical minus one point. Hence, excellent relative stability is realized since the phase margin is greater than 40 degrees.

The Bode attenuation diagram. The Bode attenuation diagram representing the balance control system is presented in Figure 16. The long minus one slope on each side of crossover insures effective noise attenuation. A series equalizing network is applicable for further attenuation of noise at frequencies between one and eighteen radians per second if needed in a specific wind-tunnel test.

The arrangement of control system components. The control system components whose values are included in the loop gain function and the closed-loop transfer function are shown as arranged in Figure 17. Those components in the feedback path are the LVDT, the integrator, the tachometer, and the tachometer amplifier.

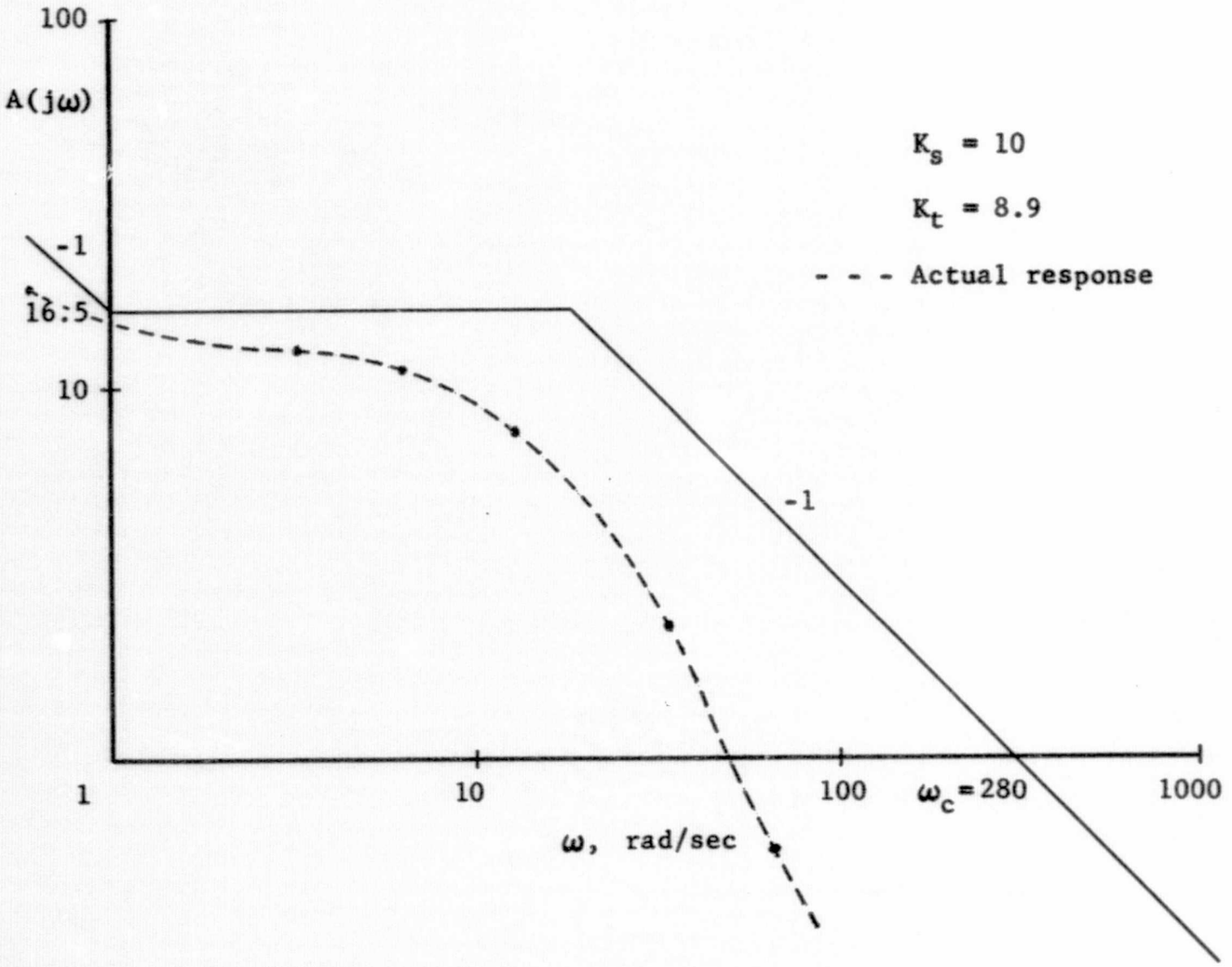

Figure 16. Bode attenuation diagram for the balance control system.

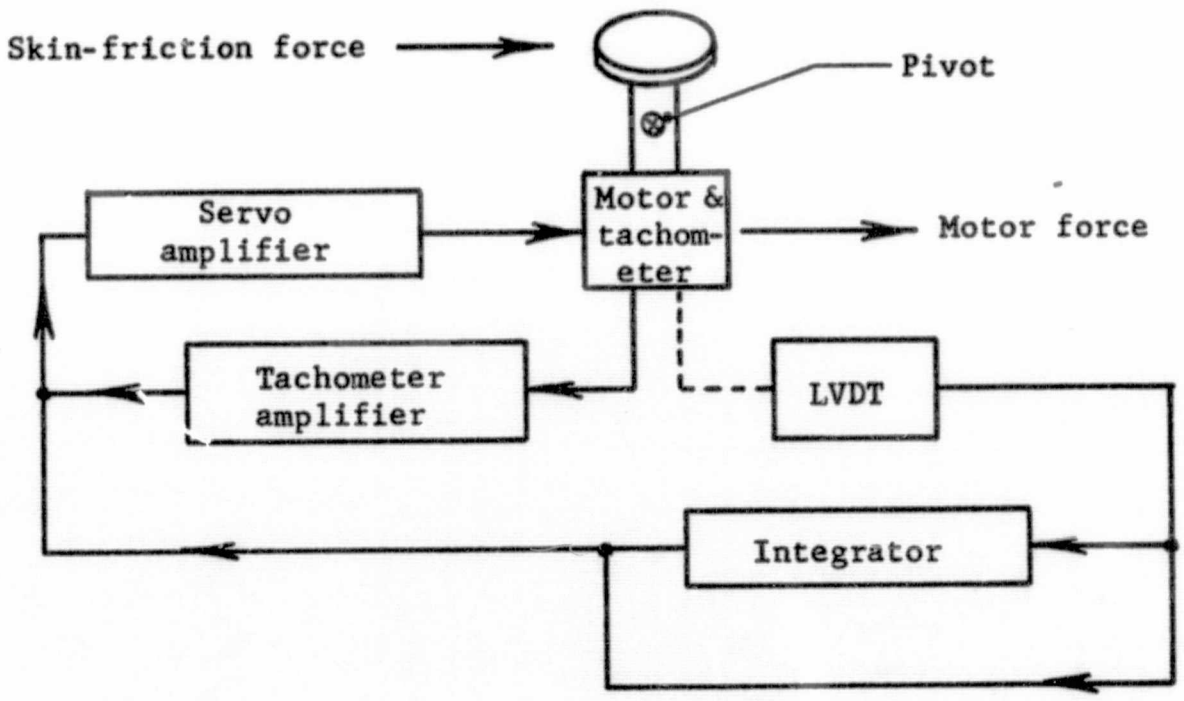

Figure 17. Block representation showing the arrangement of balance control system components.

CHAPTER V

BALANCE PERFORMANCE

Laboratory experiments have demonstrated some of the balance performance characteristics. Initial control system tests were conducted on the bench with the apparatus presented in Figure 18. Bench tests were necessary in order to debug the control system before final assembly.

Balance calibration. Calibration loads using deadweights were applied along the sensitive axis of the balance tangent to the sensing element surface. Even load increments of one-tenth pound were applied in ascending and descending order to produce the calibration curve depicted in Figure 19. The maximum load capacity of the balance is 0.45 pound or ten per cent less than specified. At 0.45 pound the servo amplifier output is one ampere which is the maximum rated output.

Balance nonrepeatability and nonlinearity. Nonrepeatability, including hysteresis, of the balance output is 0.14 per cent of full scale. Nonlinearity, defined as the maximum departure of the calibration curve from the straight line between extreme end points, is 0.71 per cent of full scale. These results are representative of data from the single calibration load cycle presented in Figure 19.

Balance resolution. Balance resolution is defined as the minimum load change which the balance will detect. Resolution of the

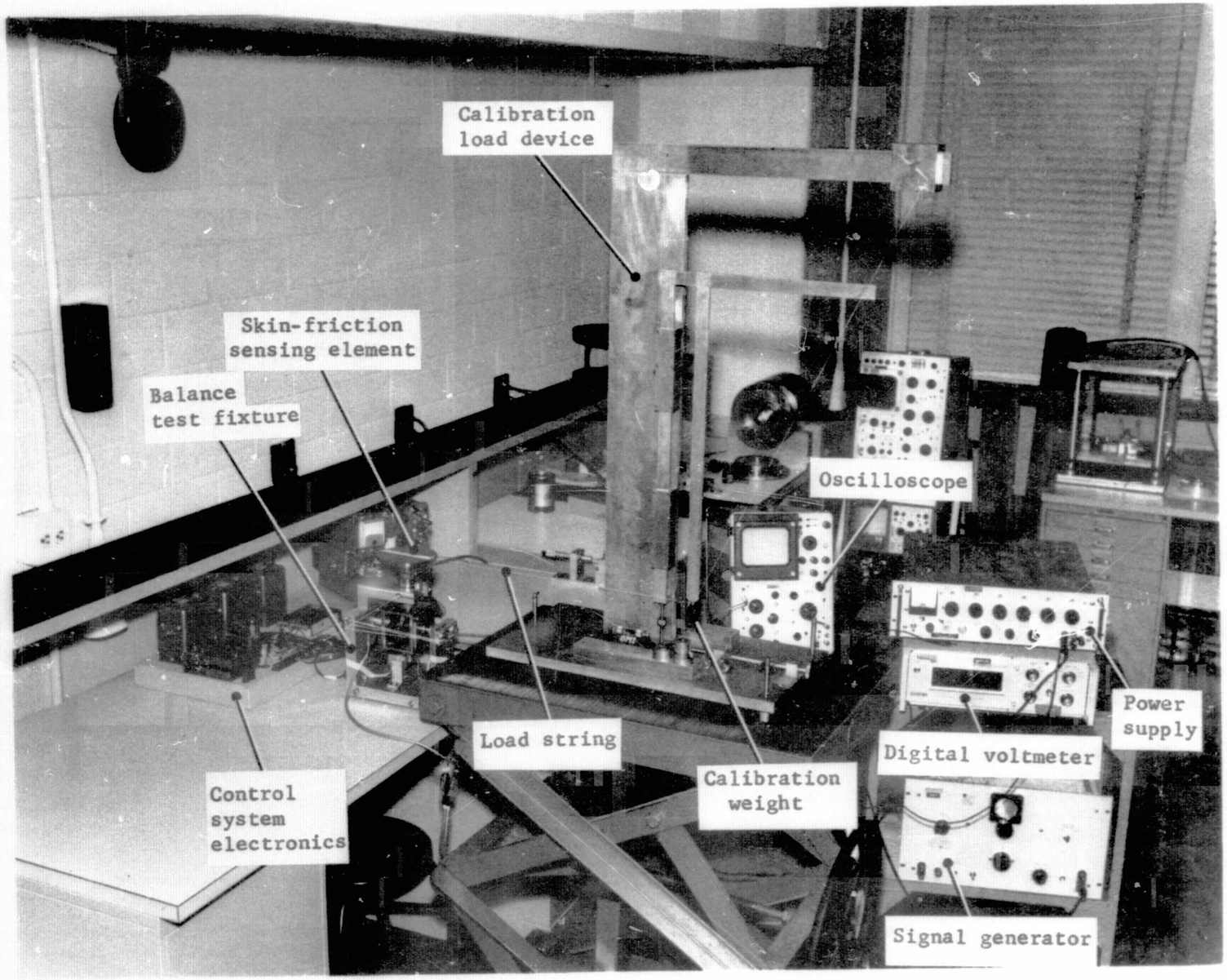

Figure 18. Control system test apparatus.

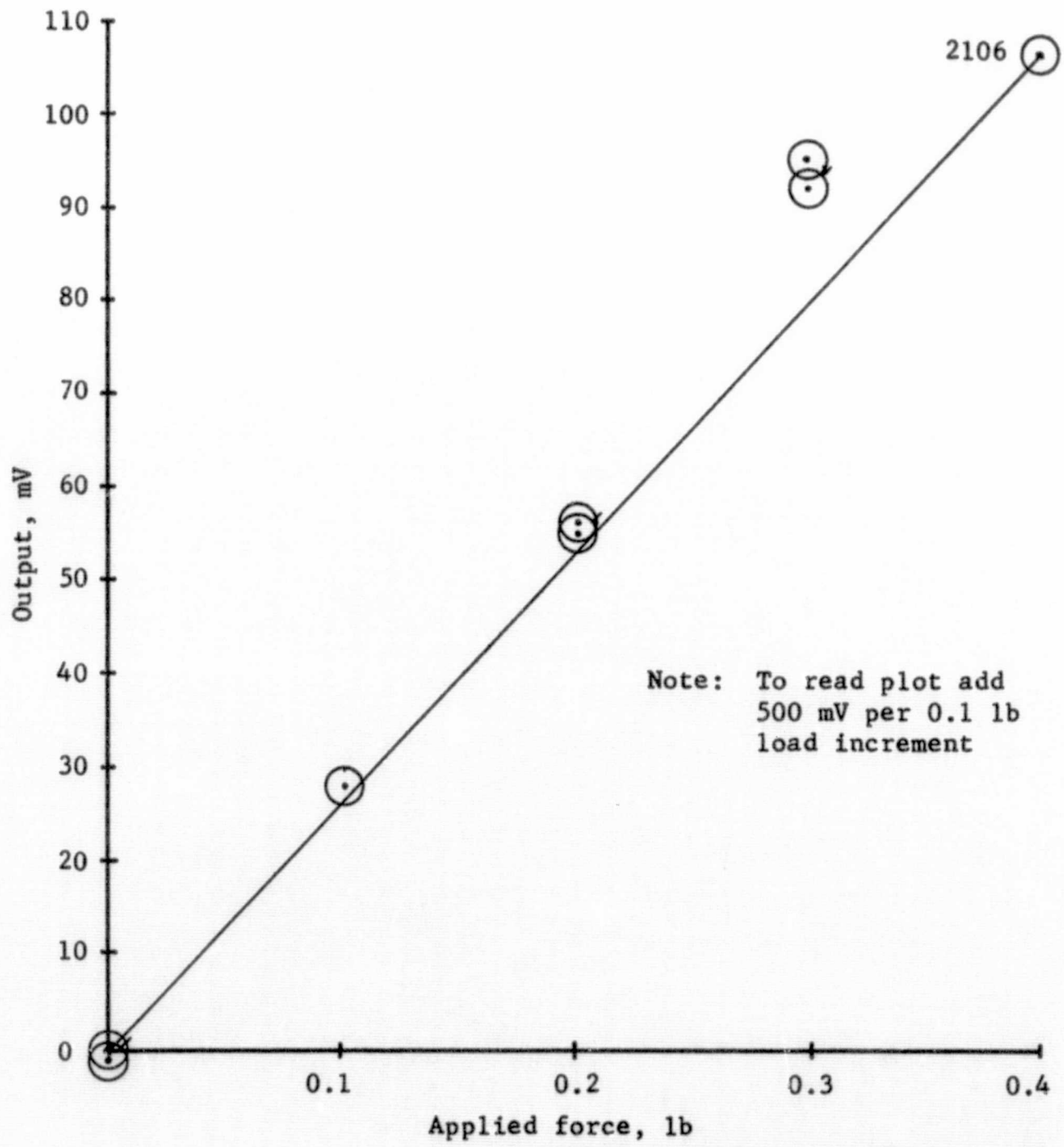

Figure 19. Balance calibration curve.

balance is less than one hundred ten micropounds as determined at room conditions. The resolution is limited by noise in the output signal.

Balance frequency response. The experimental frequency response curve presented in Figures 16 and 20 establish actual crossover at fifty rad/sec. The difference between the actual crossover at fifty rad/sec and the theoretical crossover at two hundred fifteen rad/sec is attributed to more phase lag than predicted at frequencies above the eighteen rad/sec resonant frequency. This is evident by the rapid attenuation rate on the frequency response curve. The additional phase lag is most likely contributed by one or more system components considered previously to have zero or negligible effect. Good relative stability is retained and the higher attenuation rate is desirable, consequently the lower crossover frequency imposes no serious limitations on the intended balance application.

Balance step force input response. Step force input response of the balance is presented in Figure 21 for K_t equal to 8.9, 11, and 15. The subsequent balance response time when K_t equals 8.9 is six hundred milliseconds, where response time is defined as the time required for the output to remain within ninety per cent of the final value. The rise time for K_t equal to 8.9 is forty milliseconds, where rise time is defined as the time required for the output ramp to go from ten per cent to ninety per cent of the final value. With K_t equal to fifteen the additional equivalent damping gives an improvement in response to the extent that only one cycle of overshoot is realized.

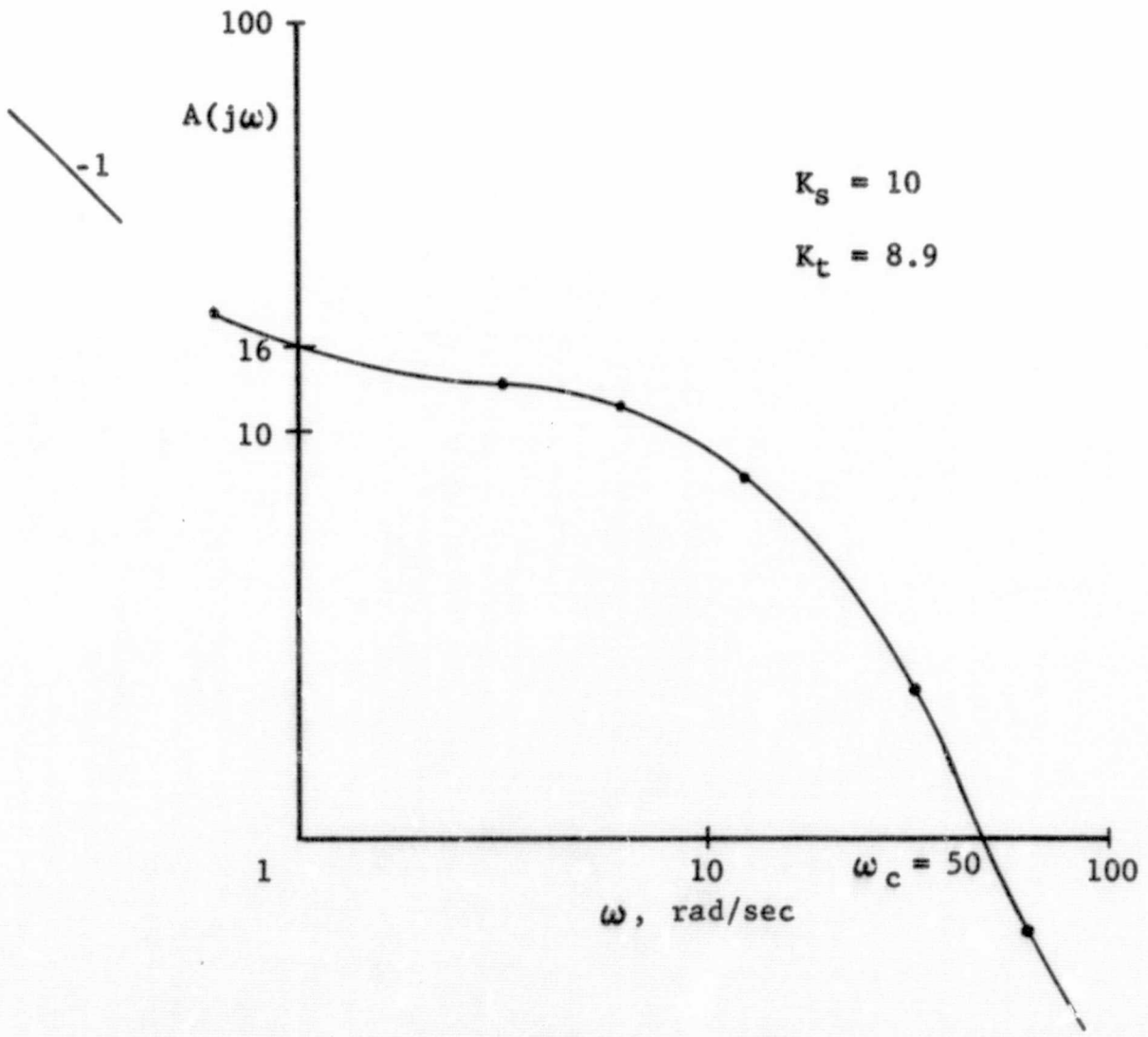

Figure 20. Balance frequency response curve.

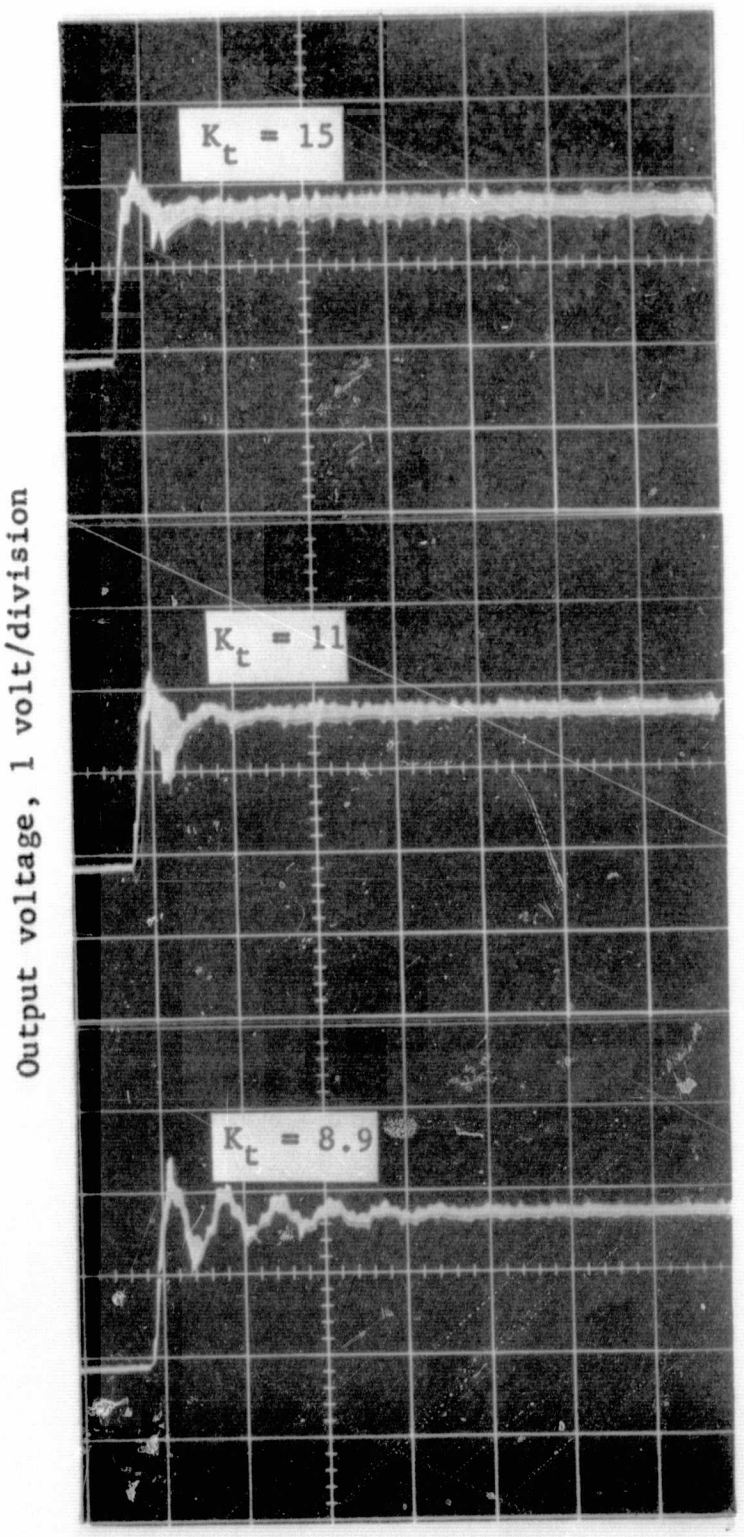

Figure 21. Balance step force input response.

Any value of K_t between 8.9 and 15 will consequently result in good relative stability as predicted by theory.

Photographs of the completed balance. Figure 22 presents the disassembled balance with each part located adjacent to its neighbor in the assembled configuration. The assembled balance is presented in Figure 23. Here the top half of the mounting flange has been removed. In this configuration the sensing element is accessible for cleaning and for replacement with another element. Figure 24 shows the balance completely assembled. The completed balance weighs approximately one hundred forty pounds.

This chapter has presented some of the balance performance characteristics. These results ascertain that the primary design objectives are met.

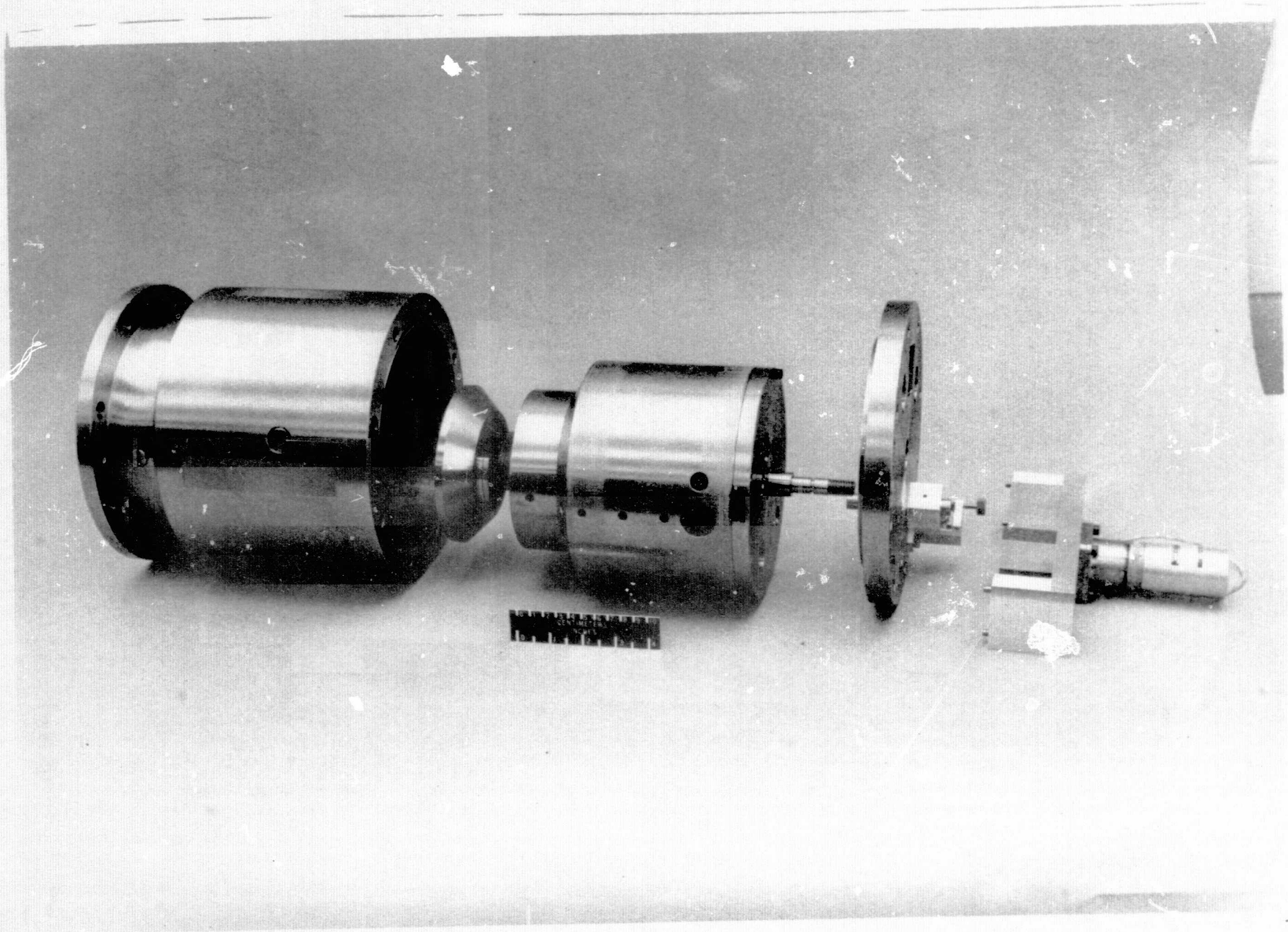

Figure 22. Disassembled skin-friction balance.

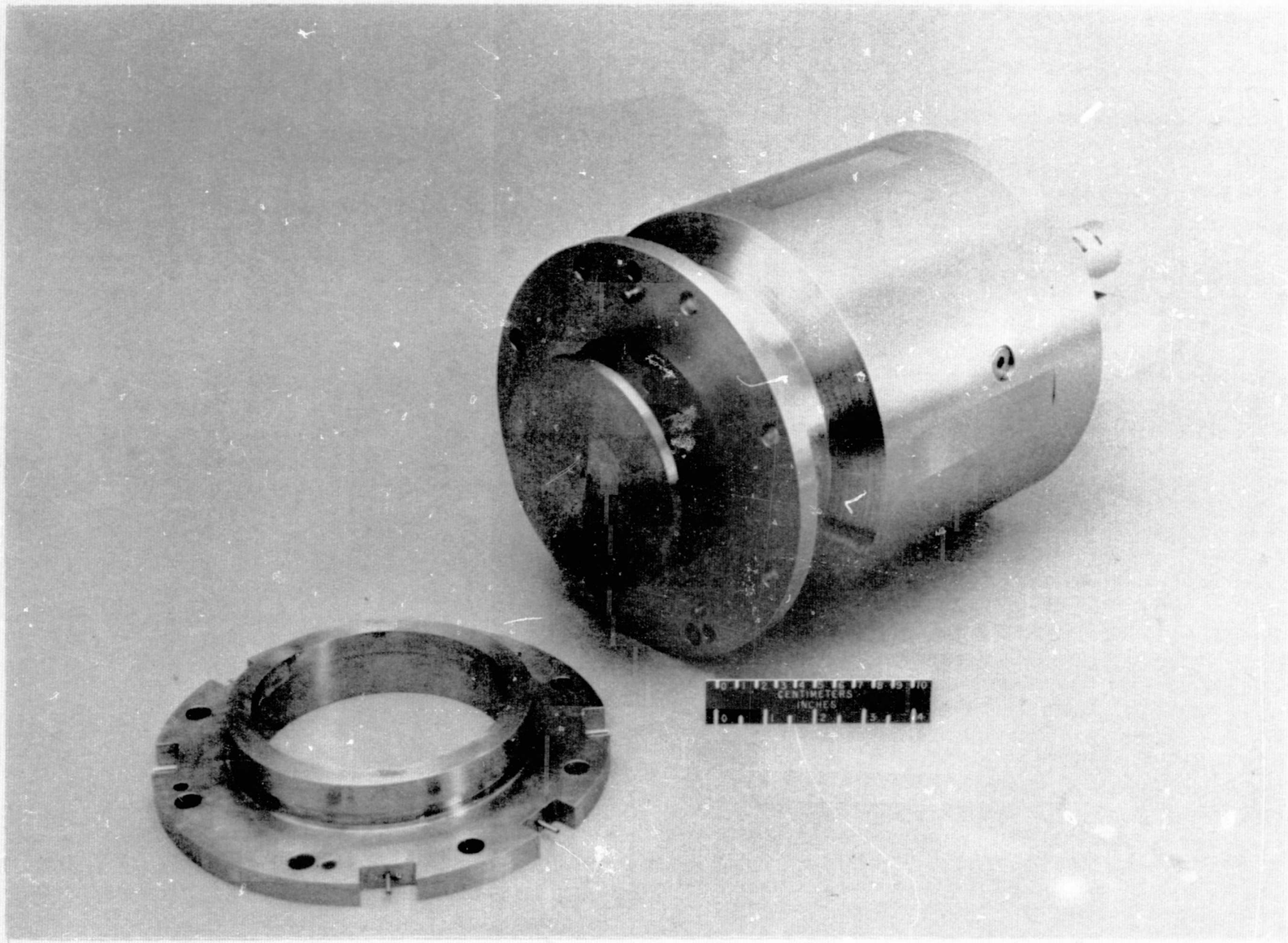

Figure 23. Assembled skin-friction balance with top half of mounting flange removed.

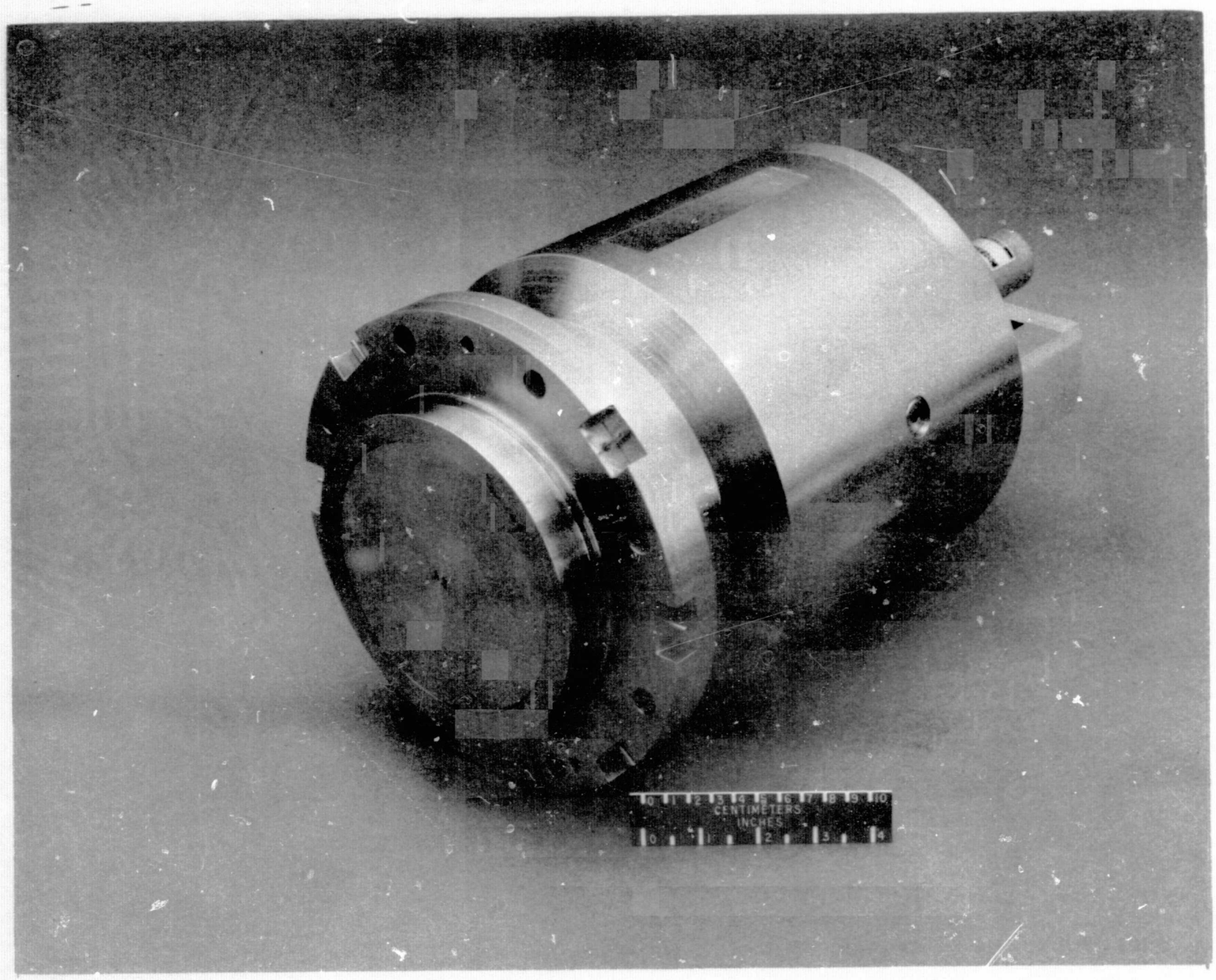

Figure 24. Assembled skin-friction balance.

CHAPTER VI

CONCLUDING REMARKS

Balance data obtained in the laboratory indicate that the balance design objectives can be met. Additional experiments and adjustments are necessary to fully evaluate balance performance and to satisfy all of the design goals. This unique balance will serve as a useful tool enabling experiments to further explore uncertainties associated with direct skin-friction measurements. Contingent upon these findings are which of the included balance design and wind-tunnel test considerations are influential in contributing significant attendant measurement errors. These findings will contribute toward a better understanding of the uncertainties which are inherent in some skin-friction experiments. Additionally, results obtained with this instrument in the wind tunnel will help to establish new skin-friction balance design criteria and will contribute toward the formulation of new skin-friction theories.

Recommendations

Based on the results obtained in the laboratory with the skin-friction balance, the most appropriate areas for further work are considered to be:

1. Replace the present force motor with one having at least twenty per cent more flux in the radial flux field. The additional flux is needed to realize one-half pound capacity at one ampere.

Machining of the present magnet to increase clearance between the pole pieces and the voice coil is deemed responsible for lowering the motor force constant.

2. Investigate the effect of temperature on balance sensitivity and zero drift. These characteristics are needed to correct balance data when environmental changes occur.

3. Insert an attenuator in the readout circuit to reduce the output to one hundred millivolts as required by wind-tunnel instrumentation.

BIBLIOGRAPHY

1. Hopkins, Edward J.; and Keener, Earl R.: Study of Surface Pitots for Measuring Turbulent Skin Friction at Supersonic Mach Numbers - Adiabatic Wall. NASA TN D-3478, July 1966.

2. Peterson, John B., Jr.: A Comparison of Experimental and Theoretical Results for the Compressible Turbulent-Boundary-Layer Skin Friction With Zero Pressure Gradient. NASA TN D-1795, March 1963.

3. Monta, William J.; and Allen, Jerry M.: Local Turbulent Skin-Friction Measurements on a Flat Plate at Mach Numbers From 2.5 to 4.5 and Reynolds Numbers up to 69×10^6. NASA TN D-2896, July 1965.

4. Moulic, E. S.: Flat Plate Skin Friction in Low Density Hypersonic Flow-Preliminary Results. University of California, February 1963.

5. Stutts, W. H.; Hartwig, W. H.; and Weiler, J. E., Sr.: Final Report on Turbulent Boundary-Layer and Skin Friction Measurements on a Smooth, Thermally Insulated Flat Plate at Supersonic Speeds. Defense Research Laboratory, University of Texas, January 1955.

6. Fenter, F. W.; and Lyons, W. C., Jr.: The Direct Measurement of Local Skin Friction on Aerobee-Hi Rockets in Free Flight. Defense Research Laboratory, University of Texas, May 1957.

7. Weiler, J. E., Sr.: Design of an Acceleration Insensitive Skin Friction Balance for Flight Testing. Defense Research Laboratory, University of Texas, June 1954.

8. Matting, Fred W.; Chapman, Dean R.; Nyholm, Jack R.; and Thomas, Andrew G.: Turbulent Skin Friction at High Mach Numbers in Air and Helium. NASA TR R-82, 1961.

9. Coles, Donald: Measurements of Turbulent Friction on a Smooth Flat Plate in Supersonic Flow. Journal of the Aeronautical Sciences, Vol. 21, July 1954, pp. 433-448.

10. Dhawn, S.: Direct Measurements of Skin Friction. NACA TN 2567, January 1952.

11. Smith, Donald W.; and Walker, John H.: Skin Friction Measurements in Incompressible Flow. NASA TR R-26, 1959.

12. MacArthur, R. C.: Transducer for Direct Measurement of Skin Friction in the Hypersonic Shock Tunnel. CAL Report No. 129, August 1963.

13. Van Kuren, James T.: Development of a Skin Friction Gage for High Temperature Hypersonic Flow. Report for the 28th Meeting of the Supersonic Tunnel Association, Air Force Flight Dynamics Laboratory, Wright-Patterson Air Force Base, Ohio, October 1967.

14. Moore, James W.; McVey, Eugene S.; and Seemuller, William W.: The Design of a Skin Friction Meter for Use in Extreme Environmental Conditions. Research Laboratories for the Engineering Sciences, University of Virginia, Report Number EME-4029-103B-66U, August 1966.

15. Korkegi, Robert H.: Transition Studies of Skin Friction Measurements on an Insulated Flat Plate at a Mach Number of 5.8. Journal of the Aeronautical Sciences, Volume 23, Number 2, pp. 97-107, February 1956.

16. O'Donnell, F. B.; and Westkaemper, John C.: Measurements of Errors Caused by Misalinement of Floating-Element Skin Friction Balances. University of Texas, July 1964.

17. Westkaemper, John C.: Step Temperature Effects on Direct Measurements of Drag. University of Texas, May 1963.

18. Harrison, Howard L.; and Bollinger, John G.: Introduction to Automatic Controls. International Textbook Co., 1964.

19. Pope, Alan; and Gain, Kennith L.: High-Speed Wind Tunnel Testing. John Wiley and Sons, 1965.

20. Alloy Digest, Engineering Alloys Digest, Inc., March 1964.

21. Technical Information for Bendix 'Free Flex' Pivots, The Bendix Corporation, Publication Number 19U-6-629A.

22. Cook, Nathan H.; and Robinowicz, Ernest: Physical Measurement and Analysis. Addison-Wesley Publishing Company, 1963.

23. Bower, John L.; and Schultheiss, Peter M.: Introduction to the Design of Servomechanisms. John Wiley and Sons, Inc.

24. Brown, Aubrey I.; and Marco, Salvatore M.: Introduction to Heat Transfer. McGraw-Hill Book Company, Inc., Third Edition, 1958.

APPENDIX A

Thermal insulators in the balance arm reduce heat loss by conduction from the sensing element to the balance arm and frame. Insulation also serves to reduce heat transfer to the motor and tachometer magnets. Thermal insulation is in the form of two quartz inserts in the balance arm. The quartz inserts measure one-half inch long and have the same cross-sectional area as the balance arm. One insert is installed on each side of the arm pivot axis.

Heat conduction from an installed skin-friction sensing element at two hundred degrees Fahrenheit through a single quartz insulator is given by (ref. 24)

$$q = \frac{kA\Delta T}{x} \tag{A1}$$

Assuming that the other balance parts are at a temperature of seventy degrees Fahrenheit, heat conduction from the sensing element by equation (A1) is

$$q = \frac{(9.3)(1.2 \times 10^{-2})(130)}{(0.5)} = 29.0 \text{ Btu/hr}$$

With a typical sensing element which weighs four and a quarter pounds, the loss of heat at a rate of twenty-nine Btu/hr represents a decrease in temperature from two hundred degrees Fahrenheit to one hundred forty-five degrees Fahrenheit in one hour. This assumes that the sensing element is preheated to an elevated temperature of two hundred degrees Fahrenheit and allowed to reach thermal equilibrium by

conduction only to the balance arm and frame through one insulator. The decrease in sensing element temperature will be about one degree per minute during tests of a few minutes duration.

APPENDIX B

This appendix treats the derivation of control system equations which lead to the overall system transfer functions and block diagrams presented in Chapter IV. The analysis follows that of standard text-book methods using Laplace transform techniques.

The differential equation of motion for the balance arm is

$$J\ddot{\theta} + C\dot{\theta} + K\theta = (F_m + F_a)L \tag{B1}$$

Motor force F_m is directly proportional to armature current and is expressed as

$$F_m = K_m i \tag{B2}$$

Output voltage from the LVDT (position sensor) is directly related to small balance arm displacements as

$$E_\ell = L_1 \theta K_\ell \tag{B3}$$

The schematic drawing of Figure 10 depicts the relationships between the quantities of force, length, and angle listed in equation (B3).

Tachometer output voltage is expressed as

$$E_t = K_t' K_v L\dot{\theta} \tag{B4}$$

Input voltage to the force motor is written as

$$E_m = IR \tag{B5}$$

The inductance term and the back emf term have been omitted in equation (B5) since these terms are small and consequently negligible. Solving equation (B5) for current

$$I = \frac{E_m}{R} \tag{B6}$$

Motor voltage is expressed differently from above as

$$E_m = K_s(E_r - E_s) \tag{B7}$$

Voltage E_s is the sum of voltages from the integrator, the LVDT, and the tachometer and is expressed as

$$E_s = E_i + E_\ell + E_t \tag{B8}$$

Equation (B7) is rewritten in terms of equation (B8) as

$$E_m = K_s(E_r - E_i - E_\ell - E_T) \tag{B9}$$

The motor voltage E_m is rewritten in terms of the physical constants as

$$E_m = K_s\left[E_r - K_\ell L_1 \theta(K_i + 1) - K_T L\dot{\theta}\right] \tag{B10}$$

where $E_\ell = K_\ell L_1 \theta$, $E_i = K_i E_\ell$, and $K_T = K_T' K_v$.

Equations (B1) through (B10) are transformed from the time domain to the frequency domain by the Laplace transform method. Equation (B1) becomes

$$(Js^2 + Cs + K)\theta(s) = \left[F_a(s) + F_m(s)\right]L \tag{B11}$$

The transfer function for the balance arm is obtained from equation (B10) as

$$\frac{\theta(s)}{F_a(s) + F_m(s)} = \frac{\frac{L}{J}}{s^2 + \frac{C}{J}s + \frac{K}{J}} \tag{B12}$$

Rewriting $F_m(s)$ in terms of motor current, equation (B11) becomes

$$\frac{\theta(s)}{F_a(s) + K_m I(s)} = \frac{\frac{L}{J}}{s^2 + \frac{C}{J}s + \frac{K}{J}} \tag{B13}$$

The motor transfer function is obtained from equation (B2) as

$$\frac{F_m(s)}{I(s)} = K_m \tag{B14}$$

In a similar manner, the transfer function for the LVDT is determined from equation (B3) as

$$\frac{E_\ell(s)}{L_1\theta(s)} = K_\ell \tag{B15}$$

Equation (B5) is transformed to give the motor current as

$$I(s) = \frac{E_m(s)}{R} \tag{B16}$$

The Laplace transform of equation (B10) is

$$E_m(s) = K_s\left[E_r(s) - K_\ell L_1\left(\frac{K_i}{s} + 1\right)\theta(s) - K_t Ls\theta(s)\right] \tag{B17}$$

The term $\left(\frac{K_i}{s} + 1\right)$ in equation (B17) is simplified to give

$$\left(\frac{K_i}{s} + 1\right) = K_i\left(\frac{\tau s + 1}{s}\right) \tag{B18}$$

where $\tau = \frac{1}{K_i} = 1$ second.

The term $K_i\left(\frac{\tau s + 1}{s}\right)$ represents a control action which is referred to as proportional-plus-integral control (ref. 20). This operation is performed with a single operational amplifier.

Equation (B17) is rewritten as

$$E_m = -K_s\left[K_i K_\ell L_1\left(\frac{\tau s + 1}{s}\right)\theta(s) + K_T L s\theta(s)\right] \tag{B19}$$

where E_r is zero.

The block diagrams of Figures 11 through 14 were constructed from the above equations (B10) through (B18). In turn, the control system transfer functions, G and H, were obtained from the block diagrams.